arXiv:1611.05798v1 [cond-mat.mtrl-sci] 17 Nov 2016

Evidence for a common origin of spin-orbit torque and the Dzyaloshinskii-Moriya interaction at a $Ni_{80}Fe_{20}$/Pt interface

Andrew J. Berger,[1,*] Eric R. J. Edwards,[1] Hans T. Nembach,[1] Justin M. Shaw,[1] Alexy D. Karenowska,[2] Mathias Weiler,[3,4] and Thomas J. Silva[1]

[1] *Quantum Electromagnetics Division, National Institute of Standards and Technology, Boulder, CO 80305, U.S.A.*[†]
[2] *Department of Physics, University of Oxford, Oxford, U.K.*
[3] *Walther-Meißner-Institut, Bayerische Akademie der Wissenschaften, Garching, Germany*
[4] *Physik-Department, Technische Universität München, Garching, Germany*

(Dated: November 18, 2016)

* andrew.berger@nist.gov
† Contribution of the National Institute of Standards and Technology; not subject to copyright.

Harnessing spin-charge conversion through current-driven spin torques[1,2] and spin precession-driven charge currents[3–6] is widely regarded as a key for the development of scalable and efficient spintronic devices. These conversion processes occur across ferromagnet/normal metal (FM/NM) interfaces with strong spin-orbit coupling (SOC), but details of the underlying physics are still much debated. SOC also underlies the interfacial Dzyaloshinskii-Moriya interaction (DMI)[7,8]. While efficient spin-charge conversion and large DMI often coincide, e.g., Refs. 9,10, a causal connection between these two phenomena has not yet been experimentally established. It was recently proposed that a Rashba Hamiltonian operative at a FM/NM interface gives rise to both spin-orbit torques (SOT) and DMI, such that the presence of one effect implies the other[11]. Despite the complexity of interfacial spin interactions[12], this theory provides a simple, testable quantitative relation between the DMI and SOT. Here, we use a powerful new microwave spectroscopy method to detect inverse spin-charge conversion processes in FM/NM bilayers and demonstrate that the magnitude of the SOT is in good agreement with the theoretical prediction based on the previously measured value of DMI in identical bilayers[13].

Spin-charge transduction effects for FM/NM multilayers couple electric fields to magnetic torques in the forward process (so-called spin-orbit torque (SOT)), and they couple magnetization dynamics to currents in the inverse process (iSOT). In general, these torques can be phenomenologically separated into two components: damping-like and field-like. Both are perpendicular to the FM magnetization, but the damping-like torque is odd under time-reversal and dissipative, whereas the field-like torque is even under time-reversal and conservative[14]. A classic example of a field-like torque is the action of an Oersted field on a FM magnetization due to a charge current in an adjacent conducting layer. By Onsager reciprocity, the inverse process is captured by Faraday's law: magnetization dynamics in the FM generate charge currents in the NM. More recently, it has been found that SOC in multilayers can give rise to both field- and damping-like SOTs[2,15], but with substantially different scaling than that achieved with Oersted fields. Unlike the Oersted effect, these spin-orbitronic effects are short-range, making them highly advantageous for microelectronic applications that require device scaling to high densities such as nonvolatile memory and alternative state-variable logic[16,17].

Damping-like torques due to the spin Hall effect (SHE) in heavy NM layers such as Pt and β-Ta are well-studied and understood[16,18–20]. Substantial field-like torques have also been measured for FM/NM interfaces in the forward configuration[2,9,21,22]. The Rashba-Edelstein effect (REE)[23,24] has been invoked to explain these results, since this would produce a field-like torque, but the fundamental origin of the REE in metallic multilayers remains uncertain. For example, unlike Bi, Pt does not have an intrinsic Rashba splitting[25]. Furthermore, an inverse measurement of the field-like torque in $Ni_{80}Fe_{20}$/Pt has not yet been reported. Kim, Lee, Lee, and Stiles (KLLS)[11] have shed light on the issue by showing that SOT and the Dzyaloshinskii-Moriya interaction (DMI) at a FM/NM interface are both manifestations of an underlying Rashba Hamiltonian, and predict a straightfoward relationship between the Rashba parameter α_{R}, interfacial DMI strength $D_{\mathrm{DMI}}^{\mathrm{int}}$, and the interfacial field-like SOT per spin t_{fl}:

$$\alpha_{\mathrm{R}} = \frac{\hbar^2}{2m_{\mathrm{e}}}\left(\frac{D_{\mathrm{DMI}}^{\mathrm{int}}}{2A}\right) = \frac{\hbar}{m_{\mathrm{e}}}\left(\frac{t_{\mathrm{fl}}}{v_{\mathrm{s}}}\right) \tag{1}$$

where $\hbar$ is Planck's constant divided by 2π, m_{e} is the electron mass, A is the exchange stiffness, and v_{s} is the conduction electron spin velocity (see SI for further discussion).

In this letter, we present simultaneous measurements of inverse field-like and damping-like torques in $Ni_{80}Fe_{20}$/Pt bilayers and find that Eq. 1 provides an accurate prediction for the magnitude and sign of the field-like SOT in a sample system where the ratio $D_{\mathrm{DMI}}^{\mathrm{int}}/A$ has been measured over a wide range of FM thickness[13]. Our quantification of the iSOT relies on phase-sensitive microwave transmission spectroscopy and subsequent analysis of the complex inductance of the sample, which arises from both the FM magnetization dynamics and the superposition of all AC charge currents flowing in the sample. As explained in the Methods section, the determination of the phase of all AC charge currents generated in the FM/NM bilayers, combined with Onsager reciprocity for the specific phenomenology of these measurements, is a powerful advantage of this technique that allows us to accurately identify the processes that contribute to spin-charge conversion.

We measured the ferromagnetic resonance (FMR) in metallic stacks consisting of substrate/Ta(1.5)/$Ni_{80}Fe_{20}$(3.5)/NM/Ta(3) and inverted stacks of substrate/Ta(1.5)/NM/$Ni_{80}Fe_{20}$(3.5)/Ta(3) (where the numbers in parentheses indicate thickness in nanometers). We focus on a Pt(6) NM layer due to its large intrinsic SOC, and use Cu(3.3) as a control material with nominally negligible SOC[3,26,27]. The broadband, phase-sensitive FMR measurements utilize a coplanar waveguide (CPW) as both the excitation and detection transducer. As discussed in the Methods section, any source of AC magnetic flux generated by the bilayer is inductively detected in the CPW. Therefore, the inductive load that the sample contributes to the CPW circuit consists of four terms: (1) The real-valued L_0 due to the oscillating magnetic dipolar fields produced by the resonating $Ni_{80}Fe_{20}$(Permalloy, Py) magnetization, (2) the Faraday-effect

currents induced in the NM layer by the precessing Py magnetization, (3) currents produced by damping-like iSOT effects (e.g., spin pumping + iSHE), and (4) currents produced by field-like iSOT effects (e.g., REE). The latter three inductances, which we collectively define as complex-valued L_{NM}, are produced by currents in the NM which generate Oersted fields that inductively couple to the CPW. Since these currents are in response to a driving force (here, the time-derivative of the precessing magnetization, $\partial_t \hat{m}$), we quantify them with the effective conductivities $\sigma_{\mathrm{e}}^{\mathrm{F}}$, $\sigma_{\mathrm{o}}^{\mathrm{SOT}}$, and $\sigma_{\mathrm{e}}^{\mathrm{SOT}}$. Here, the superscripts indicate the source of the current as due to the Faraday effect or SOT and the subscripts indicate "even" or "odd" with respect to time-reversal, which determines the phase of the corresponding inductance with respect to the driving microwave field (see Methods). Importantly, while L_0 is independent of frequency, L_{NM} is linear in frequency, as the currents in the NM are driven by $\partial_t \hat{m}$. Hence, frequency-dependent measurements allow us to disentangle L_0 and L_{NM}.

We therefore collected room-temperature FMR spectra as a function of out-of-plane external magnetic field H_0 from 5 GHz to 35 GHz by microwave transmission S_{21} measurements with a vector network analyzer (VNA) with output power 0 dBm. Exemplary $\mathrm{Re}(\Delta S_{21})$ spectra are shown in Fig. 1. Phase and amplitude analysis of S_{21} vs. H_0 provide a measure of the complex inductance of the sample. Each raw spectrum has been normalized by the complex signal background, effectively de-embedding the sample contribution to the inductance from any (frequency-dependent) losses or phase shifts caused by the microwave cables and CPW (see Methods).

Both Py/Cu and Cu/Py samples exhibit a mostly real inductance (symmetric Lorentzian dip for $\mathrm{Re}(\Delta S_{21})$ in Fig. 1(a) and (b)) with a magnitude largely independent of frequency, in accordance with $L_{\mathrm{NM}} \approx 0$. In contrast, the lineshape and magnitude of the Py/Pt and Pt/Py data in Fig. 1(c) and (d) exhibit a clear frequency dependence as expected for $L_{\mathrm{NM}} \neq 0$. In particular, the data for Py/Pt indicate that $\mathrm{Re}(L_{\mathrm{NM}}) > 0$, such that $\mathrm{Re}(L)$ increases with increasing f. Pt/Py evolves according to $\mathrm{Re}(L_{\mathrm{NM}}) < 0$ due to the stack inversion, leading to a decrease and eventual compensation of $\mathrm{Re}(L)$ at high f. The increasingly antisymmetric lineshape for both Py/Pt and Pt/Py reveals that the magnitude of $\mathrm{Im}(L)$ also increases with frequency, with a sign given by the stacking order.

By normalizing the spectra in Fig. 1 to the magnetic susceptibility $\chi(\omega, H_0)$ defined in Eq. M15, we extract the complex inductance amplitude $\tilde{L} \equiv L/\chi_{yy}(\omega, H_0)$. $\mathrm{Re}(\tilde{L})$ and $\mathrm{Im}(\tilde{L})$ are shown in Fig. 2 for all investigated bilayers with a length l of 8 mm. The behavior of these curves is described by:

$$\mathrm{Re}(\tilde{L}) = \tilde{L}_0 + \mathrm{sgn}(\hat{z} \cdot \hat{n})\mathrm{Re}(\tilde{L}_{\mathrm{NM}}(\omega)) \tag{2}$$

$$\mathrm{Im}(\tilde{L}) = \mathrm{sgn}(\hat{z} \cdot \hat{n})\mathrm{Im}(\tilde{L}_{\mathrm{NM}}(\omega)) \tag{3}$$

Full expressions are provided in Eqs. M12 and M13 of the Methods section. Briefly, $\mathrm{Re}(\tilde{L})$ provides information about the dipolar inductance ($\tilde{L}_0$, zero-frequency intercept), and $\sigma_{\mathrm{o}}^{\mathrm{SOT}}$ (slope). Similarly, the slope of $\mathrm{Im}(\tilde{L})$ reflects $(\sigma_{\mathrm{e}}^{\mathrm{SOT}} - \sigma_{\mathrm{e}}^{\mathrm{F}})$. Immediately evident is the reversal of the slope for Py/Pt compared to Pt/Py, which is captured by the sgn function (where $\hat{n}$ is the FM/NM interface normal, pointing into the FM, and $\hat{z}$ is defined by the coordinate system in Fig. S1). This sign-reversal is consistent with the phenomenology expected for interface-symmetry sensitive effects, e.g., combined spin pumping and SHE, as well as REE. There is also a marked difference in the slope magnitude for Py/Pt and Pt/Py in panel (b), the implications of which are discussed below. After accounting for sample-to-sample variation in L_0 and measuring samples with a range of l to accurately normalize our results for sample length (both described in Methods Sec. II.D), we obtain the average values of $\sigma_{\mathrm{o}}^{\mathrm{SOT}}$ and $(\sigma_{\mathrm{e}}^{\mathrm{SOT}} - \sigma_{\mathrm{e}}^{\mathrm{F}})$ shown in Table I. The ratio of $\sigma_{\mathrm{o}}^{\mathrm{SOT}}/\sigma_{\mathrm{e}}^{\mathrm{SOT}}$ measured here is in quantitative agreement with the observation in Ref. 6—using a complimentary technique and similar samples—that the dominant contribution to AC spin-charge currents in the Py/Pt samples opposes the Faraday effect currents.

For comparison to previous measurements and to theory, we can relate these effective conductivities to microscopic spin-charge conversion parameters under the assumptions that the damping-like iSOT is due to iSHE only, and the field-like iSOT is from iREE only. First, $\sigma_{\mathrm{o}}^{\mathrm{SOT}}$ can be related to the spin Hall angle θ_{SH} (see SI). We find θ_{SH} values of 0.12 ± 0.02 and 0.15 ± 0.03 for the Py/Pt and Pt/Py samples, respectively, which falls within the range of published values from DC spin Hall measurements (0.01–0.33)[1,6,19,28–33].

For the Pt/Py stack, the ratio of interfacial DMI, $D_{\mathrm{DMI}}^{\mathrm{int}}$, to bulk exchange A was previously measured via a combination of Brillouin light scattering (BLS) and superconducting quantum interference device (SQUID) magnetometry for samples prepared under nearly identical growth conditions, albeit with a stack geometry that was optimized for optical BLS measurements[13]. The ratio is a constant value of $-0.25 \pm 0.01\,\mathrm{nm}^{-1}$ over a Py thickness range of 1.3 to 15 nm. As such, this material system is an ideal candidate to test the quantitative prediction of the KLLS theory. This experimentally-determined value for $D_{\mathrm{DMI}}^{\mathrm{int}}/A$ with Eq. 1 predicts a Rashba strength of $-4.8 \pm 0.2\,\mathrm{meV\,nm}$.

To compare our measurements with the KLLS prediction, we relate the conductivity $\sigma_{\mathrm{e}}^{\mathrm{SOT}}$ to the Rashba parameter α_{R} (derivation in SI):

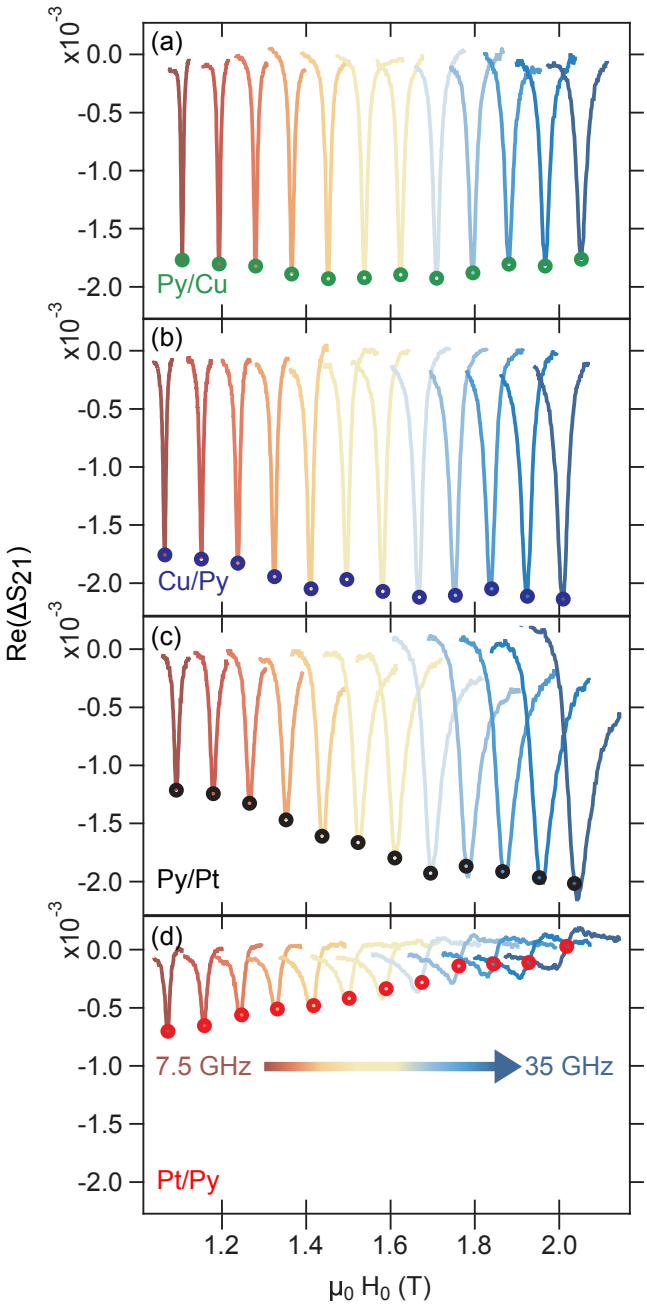

Figure 1. FMR spectra for FM/NM bilayers. $\mathrm{Re}(\Delta S_{21})$ at several excitation frequencies for different samples: (a) Py/Cu, (b) Cu/Py, (c) Py/Pt, and (d) Pt/Py. The change in lineshape and amplitude for Py/Pt and Pt/Py clearly shows the presence of frequency-dependent inductive terms not present in the Py/Cu and Cu/Py control samples. The colored circles indicate the value of $\mathrm{Re}(\Delta S_{21}) \propto \mathrm{Re}(L)$ when H_0 satisfies the out-of-plane FMR condition.

$$\alpha_{\mathrm{R}} = \frac{\hbar^2}{2m_{\mathrm{e}}} \frac{\sigma_{\mathrm{e}}^{\mathrm{SOT}}}{P d_{\mathrm{int}}} \frac{\rho_{\mathrm{int}}}{d_{\mathrm{int}}} \tag{4}$$

Here, ρ_{int} is the interfacial resistivity of the FM/NM interface (extracted by measuring resistance vs. Py thickness; see Methods) and P is the spin polarization at the FM/NM interface. We use $P = 0.6$ as determined via spin-wave Doppler measurements in Ref. 34, and assume d_{int} is one Py lattice constant (0.354 nm)[35]. Under the assumption that the discrepency in $\sigma_{\mathrm{e}}^{\mathrm{SOT}}$ seen in Fig. 2 for the two stacking orders is due to a difference in $D_{\mathrm{DMI}}^{\mathrm{int}}$, we compare the

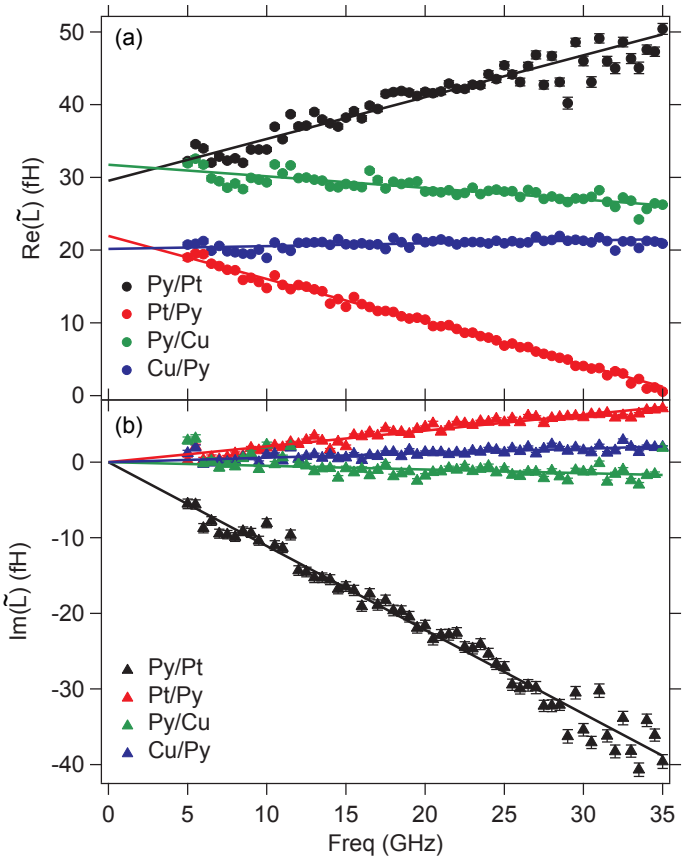

Figure 2. Frequency dependence of real and imaginary inductances extracted from S_{21} spectra (symbols) and fits to Eqs. 2 and 3 (lines). (a) $\mathrm{Re}(\tilde{L})$ for all samples with $l = 8\,\mathrm{mm}$. Zero-frequency intercept indicates the dipolar inductive coupling, while the linear slope reflects $\sigma_{\mathrm{o}}^{\mathrm{SOT}}$. (b) $\mathrm{Im}(\tilde{L})$ for all samples, as a function of frequency, where the linear slope includes contributions from both $\sigma_{\mathrm{e}}^{\mathrm{SOT}}$ and $\sigma_{\mathrm{e}}^{\mathrm{F}}$.

Sample	$\sigma_{\mathrm{o}}^{\mathrm{SOT}}$	$(\sigma_{\mathrm{e}}^{\mathrm{SOT}} - \sigma_{\mathrm{e}}^{\mathrm{F}})$	θ_{SH}	α_{R} (meV nm)
Py/Pt	0.90 ± 0.03	-1.9 ± 0.2	0.12 ± 0.02	-13 ± 1
Pt/Py	1.38 ± 0.04	-0.5 ± 0.2	0.15 ± 0.03	-3 ± 1
Py/Cu	-0.285 ± 0.007	0.1 ± 0.1		
Cu/Py	-0.07 ± 0.03	0.1 ± 0.2		

Table I. Effective conductivities and microscopic spin-charge conversion parameters (spin Hall angle θ_{SH} and Rashba parameter α_{R}). All conductivites are expressed in units of $10^5\ \Omega^{-1}\ \mathrm{m}^{-1}$.

α_{R} result from BLS measurements to that obtained from $\sigma_{\mathrm{e}}^{\mathrm{SOT}}$ measurements of the sample with identical stacking order (Pt/Py): $\alpha_{\mathrm{R}} = -3 \pm 1\,\mathrm{meV\,nm}$. If instead the interfacial resistivity ρ_{int} changes with growth-order, and because the ρ_{int} measurement provides an average value of the Py top and bottom interfaces (see Methods), we consider an average value of α_{R} for the two stacking orders: $\overline{\alpha_{\mathrm{R}}} = -8 \pm 2\,\mathrm{meV\,nm}$. The Rashba strength calculated from BLS measurements falls between these upper and lower bounds.

The Rashba interaction affects the energetics of all electrons in the system, including those responsible for the FM magnetization and those involved in electrical transport. Therefore, as shown by the KLLS theory, the Rashba interaction is responsible for both the DMI that produces chiral magnetic ordering of the FM and the REE experienced by itinerant spins that produces interfacial SOT. In Fig. 3, we graphically demonstrate the similarity between the chiral magnetization texture due to DMI (panel (a)) and the itinerant spin precession in an effective magnetic field with the Rashba symmetry $\hat{z} \times \hat{k}$, where $\hat{z}$ is the symmetry-breaking axis and $\hat{k}$ is the electron momentum direction (panel (b)-(c)). The agreement in Rashba strength α_{R} as extracted by two separate techniques—spin wave spectroscopy and inverse spin orbit torque measurements—establishes the Rashba spin-orbit interaction as the underlying physical mechanism for both DMI and field-like SOT in metallic bilayer spin-orbit systems.

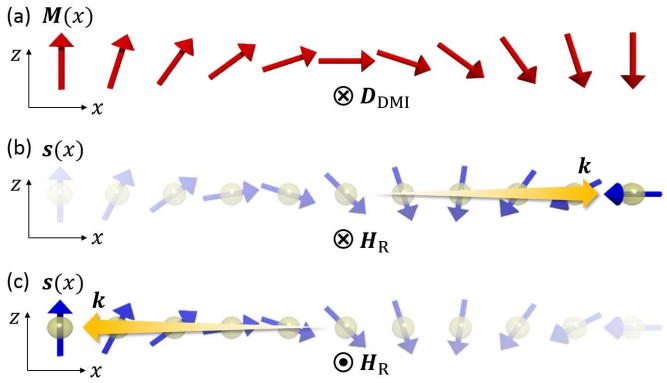

Figure 3. Connection between DMI and REE. (a) In the case of DMI, the spin-orbit field can give rise to an equilibrium magnetization distribution with a chirality characterized by the DMI vector $\mathbf{D}_{\mathrm{DMI}}$. (b,c) In the case of the REE, the spin-orbit field causes nonequilibrium precession of an itinerant spin in an effective Rashba field $\mathbf{H}_{\mathrm{R}}$. The Rashba field depends on the propagation direction of the spin ($\mathbf{H}_{\mathrm{R}} \parallel \hat{z} \times \hat{k}$), and so changes sign between (b) and (c) when the electron momentum is reversed. Therefore, the spatial chirality of the itinerant spin precession is always identical to that of the magnetization texture in (a) independent of the propagation direction of the itinerant spin.

In summary, we have quantified both field- and damping-like inverse spin-orbit torques in $Ni_{80}Fe_{20}$/Pt bilayers using phase-sensitive VNA-FMR measurements and an analysis of the sample's complex inductance that arises in part from the AC spin-charge conversion currents. The magnitude of these currents is determined by their respective SOT conductivities, a key figure of merit for characterizating and optimizing operational spintronic devices. Our new technique is a straightforward way to unpick a highly complex experimental system and represents a powerful and broadly applicable tool for studying strong SOC systems. Our measurements demonstrate that both Rashba-Edelstein and spin Hall effects must be considered in FM/NM metallic bilayers, and provide experimental evidence supporting the Rashba interaction as the common source of both iSOT and interfacial DMI in this material system. We find that the field-like iSOT can be comparable to or larger than the damping-like contribution, pointing to interfacial engineering as an opportunity for enhancing current-controlled magnetism.

ACKNOWLEDGMENTS

The authors would like to thank Mark Stiles for many helpful discussions and illuminating insights.

CONTRIBUTIONS

T.J.S. and A.D.K. conceived the experiment. A.J.B. and H.T.N. performed the VNA-FMR measurements. E.R.J.E. and J.M.S. fabricated and prepared the samples. E.R.J.E. performed the SQUID magnetometry and resistivity measurements. M.W., T.J.S., and A.J.B developed and performed the complex inductance analysis. A.J.B wrote the manuscript. All authors contributed to the interpretation of the results and editing of the manuscript.

COMPETING FINANCIAL INTERESTS

The authors declare no competing financial interests.

[1] L. Liu, T. Moriyama, D. C. Ralph, and R. A. Buhrman, Physical Review Letters **106**, 036601 (2011).
[2] I. Mihai Miron, G. Gaudin, S. Auffret, B. Rodmacq, A. Schuhl, S. Pizzini, J. Vogel, and P. Gambardella, Nature Materials **9**, 230 (2010).
[3] E. Saitoh, M. Ueda, H. Miyajima, and G. Tatara, Applied Physics Letters **88**, 182509 (2006).
[4] M. V. Costache, M. Sladkov, S. M. Watts, C. H. van der Wal, and B. J. van Wees, Physical Review Letters **97**, 216603 (2006).

[5] J. C. R. Sánchez, L. Vila, G. Desfonds, S. Gambarelli, J. P. Attané, J. M. De Teresa, C. Magén, and A. Fert, Nature Communications **4**, 2944 (2013).
[6] M. Weiler, J. M. Shaw, H. T. Nembach, and T. J. Silva, Physical Review Letters **113**, 157204 (2014).
[7] I. Dzyaloshinsky, Journal of Physics and Chemistry of Solids **4**, 241 (1958).
[8] T. Moriya, Physical Review **120**, 91 (1960).
[9] C. O. Avci, K. Garello, C. Nistor, S. Godey, B. Ballesteros, A. Mugarza, A. Barla, M. Valvidares, E. Pellegrin, A. Ghosh, I. M. Miron, O. Boulle, S. Auffret, G. Gaudin, and P. Gambardella, Physical Review B **89**, 214419 (2014).
[10] K. Di, V. L. Zhang, H. S. Lim, S. C. Ng, M. H. Kuok, X. Qiu, and H. Yang, Applied Physics Letters **106**, 052403 (2015).
[11] K.-W. Kim, H.-W. Lee, K.-J. Lee, and M. D. Stiles, Physical Review Letters **111**, 216601 (2013).
[12] V. P. Amin and M. D. Stiles, Physical Review B **94**, 104419 (2016).
[13] H. T. Nembach, J. M. Shaw, M. Weiler, E. Jué, and T. J. Silva, Nature Physics **11**, 825 (2015).
[14] F. Freimuth, S. Blügel, and Y. Mokrousov, Physical Review B **92**, 064415 (2015).
[15] Z. Duan, A. Smith, L. Yang, B. Youngblood, J. Lindner, V. E. Demidov, S. O. Demokritov, and I. N. Krivorotov, Nature Communications **5** (2014), 10.1038/ncomms6616.
[16] L. Liu, C.-F. Pai, Y. Li, H. W. Tseng, D. C. Ralph, and R. A. Buhrman, Science **336**, 555 (2012).
[17] A. Manchon, H. C. Koo, J. Nitta, S. M. Frolov, and R. A. Duine, Nature Materials **14**, 871 (2015).
[18] F. D. Czeschka, L. Dreher, M. S. Brandt, M. Weiler, M. Althammer, I.-M. Imort, G. Reiss, A. Thomas, W. Schoch, W. Limmer, H. Huebl, R. Gross, and S. T. B. Goennenwein, Physical Review Letters **107**, 046601 (2011).
[19] M. Weiler, J. M. Shaw, H. T. Nembach, and T. J. Silva, IEEE Magnetics Letters **5**, 3700104 (2014).
[20] H. L. Wang, C. H. Du, Y. Pu, R. Adur, P. C. Hammel, and F. Y. Yang, Physical Review Letters **112**, 197201 (2014).
[21] K. Garello, I. M. Miron, C. O. Avci, F. Freimuth, Y. Mokrousov, S. Blügel, S. Auffret, O. Boulle, G. Gaudin, and P. Gambardella, Nature Nanotechnology **8**, 587 (2013).
[22] X. Fan, H. Celik, J. Wu, C. Ni, K.-J. Lee, V. O. Lorenz, and J. Q. Xiao, Nature Communications **5** (2014), 10.1038/ncomms4042.
[23] Y. A. Bychkov and E. I. Rashba, JETP Letters **39**, 78 (1984).
[24] V. M. Edelstein, Solid State Communications **73**, 233 (1990).
[25] S. Souma, A. Takayama, K. Sugawara, T. Sato, and T. Takahashi, Review of Scientific Instruments **81**, 095101 (2010).
[26] Y. Niimi, M. Morota, D. H. Wei, C. Deranlot, M. Basletic, A. Hamzic, A. Fert, and Y. Otani, Physical Review Letters **106**, 126601 (2011).
[27] J. Sinova, S. O. Valenzuela, J. Wunderlich, C. H. Back, and T. Jungwirth, Reviews of Modern Physics **87**, 1213 (2015).
[28] M. Isasa, E. Villamor, L. E. Hueso, M. Gradhand, and F. Casanova, Physical Review B **91**, 024402 (2015).
[29] O. Mosendz, V. Vlaminck, J. E. Pearson, F. Y. Fradin, G. E. W. Bauer, S. D. Bader, and A. Hoffmann, Physical Review B **82**, 214403 (2010).
[30] M. Morota, Y. Niimi, K. Ohnishi, D. H. Wei, T. Tanaka, H. Kontani, T. Kimura, and Y. Otani, Physical Review B **83**, 174405 (2011).
[31] M. Weiler, M. Althammer, M. Schreier, J. Lotze, M. Pernpeintner, S. Meyer, H. Huebl, R. Gross, A. Kamra, J. Xiao, Y.-T. Chen, H. Jiao, G. E. W. Bauer, and S. T. B. Goennenwein, Physical Review Letters **111**, 176601 (2013).
[32] M. Obstbaum, M. Härtinger, H. G. Bauer, T. Meier, F. Swientek, C. H. Back, and G. Woltersdorf, Physical Review B **89**, 060407 (2014).
[33] C.-F. Pai, Y. Ou, L. H. Vilela-Leão, D. C. Ralph, and R. A. Buhrman, Physical Review B **92**, 064426 (2015).
[34] M. Zhu, C. L. Dennis, and R. D. McMichael, Physical Review B **81**, 140407 (2010).
[35] P. M. Haney, H.-W. Lee, K.-J. Lee, A. Manchon, and M. D. Stiles, Physical Review B **88**, 214417 (2013).

Methods

Because this work utilizes a new analysis technique for extracting phenomenological parameters not commonly used in literature, we provide a thorough explanation of all experimental and mathematical details for use of our quantitative VNA-FMR technique and analysis of measurements. In Sec. I, by appealing to Onsager reciprocity we provide the phenomenological background relating the forward and inverse processes that produce magnetic torques and charge flow in a ferromagnet/normal metal system under electrical bias or with excited magnetization dynamics. In Sec. II, we describe sample fabrication and preparation. Sec. III describes the quantitative VNA-FMR technique, and introduces the expressions we use to calculate the sample's complex inductance. This section also introduces the effective complex conductivity $\tilde{\sigma}_{\mathrm{NM}}$ that quantifies the magnitude and phase of the AC charge currents flowing in the sample in response to the driven magnetization dynamics. Sec. III B describes the procedure used to de-embed the sample's contribution to the VNA transmission signal. Finally, Sec. IV provides the mathematical expressions for each of the contributions to the sample inductance, and how the effective conductivity is calculated from the measured inductance.

I. THEORY

By analogy to $\mathbf{J} = \sigma\mathbf{E}$, we can write a general matrix equation relating driving forces (magnetization dynamics $\partial\hat{m}/\partial t$ and electric field $\mathbf{E}$) to flows (magnetic torque density $\mathbf{T}$ and charge current density $\mathbf{J}$)[M1]:

$$\begin{bmatrix} \left(\frac{2e}{\hbar}\right)\left[\int_{0}^{+d_{\mathrm{FM}}} \mathbf{T}(z)dz\right] \\ \left[\int_{-t_{\mathrm{NM}}}^{+d_{\mathrm{FM}}} \mathbf{J}(z)dz\right] \end{bmatrix} = \mathcal{G}\begin{bmatrix} G_{\mathrm{mag}} & \mathrm{sgn}(\hat{z}\cdot\hat{n})\left(-\sigma_{\mathrm{e}}^{\mathrm{F}} + \sigma_{\mathrm{e}}^{\mathrm{SOT}} + \sigma_{\mathrm{o}}^{\mathrm{SOT}}[\hat{m}\times]\right) \\ \mathrm{sgn}(\hat{z}\cdot\hat{n})\left(-\sigma_{\mathrm{e}}^{\mathrm{F}} + \sigma_{\mathrm{e}}^{\mathrm{SOT}} - \sigma_{\mathrm{o}}^{\mathrm{SOT}}[\hat{m}\times]\right) & -\frac{1}{Z_{\mathrm{eff}}} \end{bmatrix}\begin{bmatrix} \left(\frac{\hbar}{2e}\right)\frac{\partial\hat{m}}{\partial t} \\ \hat{z}\times\mathbf{E} \end{bmatrix} \tag{M1}$$

where $\hat{m}$ is the magnetization unit vector. The sign of the off-diagonal terms are determined by $\mathrm{sgn}(\hat{z}\cdot\hat{n})$, where $\hat{n}$ is an interface normal pointing into the FM. The coordinate unit vector $\hat{z}$ is defined by the sample placement on the CPW, as shown in Fig. S1(a). $\mathcal{G}$ is a 2×2 matrix imposing geometrical constraints: (1) magnetic torques are orthogonal to $\hat{m}$ and (2) charge currents can flow only in the x, y plane:

$$\mathcal{G} = \begin{bmatrix} [\hat{m}\times] & 0 \\ 0 & [\hat{z}\times] \end{bmatrix} \tag{M2}$$

The diagonal elements of the effective conductivity matrix describe the Gilbert damping of the FM and charge flow in the metallic bilayer in response to an applied electric field. That is,

$$\left(\frac{2e}{\hbar}\right)\left[\int_{0}^{+d_{\mathrm{FM}}} \mathbf{T}(z)dz\right] = \left(\frac{\hbar}{2e}\right) G_{\mathrm{mag}}\left(\hat{m}\times\frac{\partial\hat{m}}{\partial t}\right) \tag{M3}$$

$$\left[\int_{-t_{\mathrm{NM}}}^{+d_{\mathrm{FM}}} \mathbf{J}(z)dz\right] = -\frac{1}{Z_{\mathrm{eff}}}\hat{z}\times(\hat{z}\times\mathbf{E}) \tag{M4}$$

$$\tag{M5}$$

where $G_{\mathrm{mag}} \equiv d_{\mathrm{FM}}(2e/\hbar)^2(\alpha M_{\mathrm{s}}/\gamma)$, α is the Gilbert damping parameter, and γ is the gyromagnetic ratio, such that Eq. M3 is the usual Gilbert damping term from the Landau-Lifshitz-Gilbert equation:

$$\frac{\partial \hat{m}}{\partial t} = -\gamma\mu_0 \hat{m} \times \mathbf{H} + \left(\frac{\gamma}{M_\mathrm{s} d_\mathrm{FM}}\right) \int_0^{+d_\mathrm{FM}} \mathbf{T}(z) dz \tag{M6}$$

In Eq. M4, Z_eff is the effective frequency-dependent impedance of the bilayer. Eq. M4 reduces to Ohm's Law in the DC limit ($Z_\mathrm{eff} \to R_\square$ as $f \to 0$).

Eq. M1 is consistent with the phenomenological formulation presented by Freimuth, Bluegel, and Mokrousov[M1], although it has been expanded to include the purely electrodynamic contributions. The off-diagonal terms describe the electromagnetic reciprocity between Faraday's and Ampere's Law[M2,M3], as well as spin-orbit torques (SOT) and their inverse.

$$\left(\frac{2e}{\hbar}\right) \left[\int_0^{+d_\mathrm{FM}} \mathbf{T}(z) dz\right] = \mathrm{sgn}(\hat{z}\cdot\hat{n}) \left(\frac{\hbar}{2e}\right) \hat{m} \times \left(-\sigma_\mathrm{e}^\mathrm{F} + \sigma_\mathrm{e}^\mathrm{SOT} + \sigma_\mathrm{o}^\mathrm{SOT}[\hat{m}\times]\right)(\hat{z}\times\mathbf{E}) \tag{M7}$$

$$\left[\int_{-d_\mathrm{NM}}^{+d_\mathrm{FM}} \mathbf{J}(z) dz\right] = \mathrm{sgn}(\hat{z}\cdot\hat{n}) \left(\frac{\hbar}{2e}\right) \hat{z} \times \left(-\sigma_\mathrm{e}^\mathrm{F} + \sigma_\mathrm{e}^\mathrm{SOT} - \sigma_\mathrm{o}^\mathrm{SOT}[\hat{m}\times]\right) \frac{\partial \hat{m}}{\partial t} \tag{M8}$$

For example, in the forward process an electric field $\mathbf{E}$ produces a charge current, which by Ampere's Law produces a magnetic field. This field exerts a torque $\mathbf{T}$ on the magnetization of the FM layer. In the reverse process, magnetization dynamics $\partial_t \hat{m}$ produce an AC magnetic field, which by Faraday's Law induces a charge current $\mathbf{J}$ in the NM layer. In this way, $\sigma_\mathrm{e}^\mathrm{F}$ quantifies the reciprocity between Ampere's and Faraday's Law. Inclusion of the terms in Eq. M1 due to electrodynamic reciprocity is critical for the proper interpretation of inverse spin orbit torque experiments[M4]. Omission of these terms can cause significant errors in data interpretation[M5].

Magnetic torques from applied electric fields can in general be phenomenologically separated into two essential components: damping-like torques, which are proportional to $\hat{m} \times (\hat{m} \times (\hat{z} \times \mathbf{E}))$, and field-like torques, which are proportional to $\hat{m} \times (\hat{z} \times \mathbf{E})$, where $\hat{z}$ is the interface normal and $\mathbf{E}$ is the applied electric field. $\sigma_\mathrm{e}^\mathrm{F}$ produces a field-like torque. The constants of proportionality between applied electric field and SOTs are $\sigma_\mathrm{o}^\mathrm{SOT}$ and $\sigma_\mathrm{e}^\mathrm{SOT}$, where the subscripts "e" and "o" indicate even and odd with respect to time reversal. By employing Onsager reciprocity[M1,M6], the inverse effects can be indentified by simply replacing $\hat{z} \times \mathbf{E}$ with $(\hbar/2e)\partial_t \hat{m}$. In this reverse direction, these effects are responsible for spin-to-charge conversion (e.g., inverse spin Hall effect[M7] or Rashba-Edelstein spin galvanic effect[M8]). Note that because of the odd time-reversal symmetry for damping-like torques, $\sigma_\mathrm{o}^\mathrm{SOT}$ must be replaced by $-\sigma_\mathrm{o}^\mathrm{SOT}$ for the inverse effect.

Our use of the descriptors "even" and "odd" are different from that of Freimuth, et al.[M1], who use the symmetry of the spin orbit torques with respect to magnetization-reversal as the symmetry identifier. We instead use the symmetry of the torque with respect to time-reversal because this is the relevant symmetry with regard to the off-diagonal components in the phenomenological equation M1[M6]. Any process for which the torque is odd under time-reversal qualifies as microscopically non-reversible in the sense of Onsager reciprocity, where microscopic reversibility pertains solely to forces that are even functions of velocity, as well as position. (We also note that all axial vectors and charge conductivity are odd under time reversal.)

II. SAMPLE FABRICATION

Sample	Deposition Order
Py/Pt	Substrate/Ta(1.5)/Py(3.5)/Pt(6)/Ta(3)
Pt/Py	Substrate/Ta(1.5)/Pt(6)/Py(3.5)/Ta(3)
Py/Cu	Substrate/Ta(1.5)/Py(3.5)/Cu(3.3)/Ta(3)
Cu/Py	Substrate/Ta(1.5)/Cu(3.3)/Py(3.5)/Ta(3)

Table I. Sample deposition orders and metallization thicknesses (in nanometers).

All samples were prepared by DC magnetron sputtering in an Ar base pressure of ≈0.07 Pa (≈0.5 mTorr) and a chamber base pressure of 3×10^{-6} Pa (2×10^{-8} Torr) on 3-inch wafers of thermally oxidized (100) Si (nominal resistivity = 3 Ω cm). The wafers were rotated at 1 Hz to 2 Hz during deposition to eliminate growth-induced anisotropy,

and the sample holder was held at room temperature. All samples are grown on a 1.5 nm Ta seed layer to promote (111) textured growth, which is then followed by the FM/NM (or NM/FM) bilayer. X-ray diffraction shows that the Ta seed layer is unordered. A 3 nm Ta cap layer prevents oxidation of the FM and NM layers. It is expected that 1 nm to 2 nm of the cap layer forms the insulator TaO when exposed to air. Deposition order and film thicknesses are shown in Table I. The Pt and Cu thicknesses were chosen so that the DC conductivities (as characterized by a four-probe measurement) of the sample and control were equal, to ensure equality of Faraday induced currents. The wafers were subsequently coated with 8 µm of photoresist to provide electrical insulation from the CPW and reduce the capacitive coupling of the CPW to the metallic layers. The wafers were diced to precise sizes using an automatic dicing saw.

III. EXPERIMENTAL TECHNIQUE

Using a vector network analyzer (VNA), we measure the change in microwave transmission of a coplanar waveguide (CPW) loaded with the bilayer sample as an out-of-plane DC magnetic field ($\mathbf{H}_0 \parallel \hat{z}$) is swept through the ferromagnetic resonance (FMR) condition of the Py layer. Samples were placed flip-chip style onto the CPW (see Fig. S1), which was positioned between the pole pieces of a room-temperature electromagnet capable of producing fields up to ≈2.2 T. To reproducibly center the sample on the CPW, a custom three dimensional (3D) printed plastic alignment jig was used. This jig fit snugly atop the CPW and contained an appropriately-sized cutout into which the sample was inserted. The jig was then removed during measurements so as to not interfere with the dielectric properties of the CPW. A VNA was used to source microwave frequencies from 5 GHz to 35 GHz and measure the complex S_{21} transmission parameter. Field sweeps were repeated to average the transmission data until appropriate signal-to-noise ratio was obtained.

Typically, VNA-FMR measurements focus on the resonance field and linewidth. Our method additionally makes use of the signal magnitude in order to directly probe the AC charge currents produced by iSOT. Previous studies of AC charge currents in spin pumping experiments have relied on intricate experimental setups or techniques that suppress or are insensitive to spurious background signals[M4,M9,M10]. Our technique remains sensitive to currents induced by the Faraday effect, but is able to separate them from spin-charge conversion currents through the combination of a phase-sensitive analysis and comparison to control samples in which Pt is substituted with a Cu layer of nominally negligible intrinsic spin-orbit effects. Furthermore, because the CPW is inductively coupled to the sample, no electrical connections need to be made directly to the FM/NM sample.

The sample adds a complex inductance L in series with the impedance of the bare CPW, Z_0 (here, 50 Ω). The change in microwave transmission ΔS_{21} is therefore that of a simple voltage divider[M11]:

$$\Delta S_{21} = \frac{1}{2}\left(\frac{-i\omega L}{Z_0 + i\omega L}\right) \approx \frac{-i\omega L}{2Z_0} \tag{M9}$$

for $Z_0 >> \omega L$, where ω is the microwave frequency. The factor of $1/2$ is needed because the port 2 voltage measurement is between the CPW signal and ground (and not between port 2 and port 1). The sample inductance L reflects the total AC magnetic flux Φ produced by the sample that threads around the CPW (see discussion and Fig. S1 in SI).

In order to extract values for the SOT effects from the measured ΔS_{21}, we derive expressions for each contribution to L. We first note that the dipole contribution (which would be present for the FM alone, without the NM layer) is given by[M11]

$$L_0 = \mu_0 l \frac{d_{\mathrm{FM}}}{4W_{\mathrm{wg}}} \chi_{yy}(\omega, H_0)\eta^2(z, W_{\mathrm{wg}}) \tag{M10}$$

where μ_0 is the vacuum permeability, l the sample length, d_{FM} the FM thickness, W_{wg} the width of the CPW signal line (here, 100 µm), and $\chi_{yy}(\omega)$ the frequency-dependent magnetic susceptibility. $\eta(z, W_{\mathrm{wg}})$ is an attenuation parameter ranging from 0 to 1 to account for the finite spacing between sample and waveguide (see Sec. IV A).

The inductance due to AC currents in the NM is given by

$$L_{\mathrm{NM}} = L_{12}(z, W_{\mathrm{wg}}, l)\eta(z, W_{\mathrm{wg}}) \frac{\hbar\omega}{4M_{\mathrm{s}}e} \chi_{yy}(\omega, H_0)\tilde{\sigma}_{\mathrm{NM}} \tag{M11}$$

where $L_{12}(z, W_{\mathrm{wg}}, l)$ is the mutual inductance of the sample and CPW, which we model[M12] as two parallel current-carrying sheets with finite spacing z (see Sec. IV B and IV C for details). M_{s} is the FM saturation magnetization (in

A/m), and e is the electron charge. Here, $\tilde{\sigma}_{\rm NM} = (\sigma_{\rm o}^{\rm SOT} + i(\sigma_{\rm e}^{\rm SOT} - \sigma_{\rm e}^{\rm F}))$ is an effective (and complex) conductivity that relates the charge currents J flowing in the NM layer to the driving force $\partial_t \hat{m}$, by analogy to Ohm's Law in which charge currents are driven by an electric field: $\mathbf{J} = \sigma\mathbf{E}$. The real and imaginary components of $\tilde{\sigma}_{\rm NM}$ produce currents driven in and out of phase with $\partial_t \hat{m}$.

Reporting the effective conductivities highlights the spin-charge transduction properties in an iSOT device with microwave inputs and charge current outputs (or reciprocally, a spin torque experiment with charge current inputs and magnetization dynamics as output). In particular, comparison of the conductivities makes evident that the charge currents produced by inverse REE are comparable to and even larger than those due to inverse SHE in these devices (see Table 1).

The effective conductivities can also be related to the often-used quantity of effective flux density per unit current density[M13] $B_{\rm eff}/J$, with units of T m^2 A^{-1} via the equation $B_{\rm eff}/J = \tilde{\sigma}_{\rm NM}\hbar/(2M_{\rm s}\sigma_{\rm Pt}d_{\rm FM}e)$. However, our definition for the effective conductivity is more general insofar as it allows one to calculate the actual SOT without the need to independently determine the sample magnetization, conductivity, or actual thickness.

The different frequency dependencies of L_0 and $L_{\rm NM}$ is critical for our analysis. When normalized to $\chi_{yy}(\omega, H_0)$, L_0 is a frequency-independent inductance. $L_{\rm NM}$ has an extra factor of ω, reflecting the fact that both Faraday and SOT effects are driven by $\partial_t \hat{m}$, rather than by $\mathbf{m}(t)$ itself. The total inductance of the sample is given by $L = L_0 + L_{\rm NM}$. After normalizing by the fitted susceptibility $\tilde{L} = L/\chi_{yy}(\omega, H_0)$, the real and imaginary inductance amplitudes are given by:

$$\begin{aligned}\mathrm{Re}(\tilde{L}) = \frac{\mu_0 l}{4}\Bigg[&\frac{d_{\rm FM}}{W_{\rm wg}}\eta^2(z, W_{\rm wg}) + \mathrm{sgn}(\hat{z}\cdot\hat{n})\eta(z, W_{\rm wg}) \\ &*\frac{L_{12}(z, W_{\rm wg}, l)}{\mu_0 l}\frac{\hbar\omega}{e}\sigma_{\rm o}^{\rm SOT}\Bigg] \end{aligned} \tag{M12}$$

$$\begin{aligned}\mathrm{Im}(\tilde{L}) = \frac{\mu_0 l}{4}\Bigg[&\mathrm{sgn}(\hat{z}\cdot\hat{n})\eta(z, W_{\rm wg}) \\ &*\frac{L_{12}(z, W_{\rm wg}, l)}{\mu_0 l}\frac{\hbar\omega}{e}(\sigma_{\rm e}^{\rm SOT} - \sigma_{\rm e}^{\rm F})\Bigg] \end{aligned} \tag{M13}$$

The sgn function is introduced to account for the deposition order of Py and Pt, with $\hat{n}$ pointing from the Py/Pt interface *into* the Py. That is, when the stacking order of FM and NM are reversed, so does the sign of the SOT and Faraday currents. Eqs. M12 and M13 are linear with excitation frequency. The $f = 0$ intercept of $\mathrm{Re}(\tilde{L})$ corresponds to dipolar inductance L_0, while the intercept of $\mathrm{Im}(\tilde{L})$ is zero. The linear slope of $\mathrm{Re}(\tilde{L})$ is governed by $\sigma_{\rm o}^{\rm SOT}$, while that of $\mathrm{Im}(\tilde{L})$ is set by $(\sigma_{\rm e}^{\rm SOT} - \sigma_{\rm e}^{\rm F})$.

Because $\sigma_{\rm e}^{\rm SOT}$ and $\sigma_{\rm e}^{\rm F}$ have the same phase and frequency dependence, we use control samples where we replace the Pt with Cu, wherein it is generally accepted that both the SHE for Cu and the REE at the Py/Cu interface are negligible[M7,M14,M15]. We can then use the Py/Cu samples to independently measure both the Faraday-induced currents in the NM component of the bilayer, i.e. $\sigma_{\rm e}^{\rm F}$, and any residual Rashba effects at the Py/Ta and Cu/Ta interfaces (Ta is used as both seed and capping layer). In this case, subtraction of the time-reversal-even conductivity for the Py/Cu control samples from the time-reversal-even conductivity for the Py/Pt samples should isolate $\sigma_{\rm e}^{\rm SOT}$ specifically for the Py/Pt interface. The bilayer notation used here, as read from left-to-right, indicates the sample growth order. For example, Py/Pt indicates Py is first deposited onto the substrate, followed by Pt.

The analysis of the data presented here presumes that the detection of the currents in the FM/NM stacks is strictly moderated by inductive coupling. In practice this is born out by the linearity of the normalized inductances presented in Fig. 2. If a thick photoresist spacing layer is not employed, the data (not shown) do not generally display the degree of linearity over the entire 30 GHz range of measurement that we obtain when the spacer layer is used. We presume that deviations from linearity are the result of parasitic capacitive coupling that complicates the signal response when the metallic sample shields the magnetic fields generated by the waveguide. Finite element modeling has shown that such shielding effects for large sample-CPW spacings are only important at frequencies greater than 35 GHz for films such as ours with a sheet resistance of 8 Ω per square[M16].

A. Magnetic Susceptibility

For our geometry, the driving microwave magnetic field lies primarily along $\hat{y}$, and we are concerned with the AC component of magnetization along $\hat{y}$ (see Fig. S1 for coordinate system). Therefore, the S_{21} spectra are fit to the

χ_{yy} component of the complex magnetic Polder susceptibility tensor in order to extract resonance field, linewidth, amplitude, and phase.

$$\begin{bmatrix} M_x \\ M_y \end{bmatrix} = \begin{bmatrix} \chi_{xx} & \chi_{xy} \\ \chi_{yx} & \chi_{yy} \end{bmatrix} \begin{bmatrix} H_x \\ H_y \end{bmatrix} \tag{M14}$$

$$\chi(\omega, H_0) = \frac{M_\mathrm{s}}{\left((H_0^2 - M_\mathrm{eff}^2) - \left(\frac{\omega}{\gamma\mu_0}\right)^2 - i\frac{2\alpha_\mathrm{eff}\omega(H_0 - M_\mathrm{eff})}{\gamma\mu_0} \right)} \begin{bmatrix} (H_0 - M_\mathrm{eff}) & -i\frac{\omega}{\gamma\mu_0} \\ i\frac{\omega}{\gamma\mu_0} & (H_0 - M_\mathrm{eff}) \end{bmatrix} \tag{M15}$$

where H_0 is the externally applied DC field, $M_\mathrm{eff} = M_\mathrm{s} - H_\mathrm{k}^\perp$ is the effective magnetization, $H_\mathrm{k}^\perp$ is the perpendicular anisotropy field, ω is the driving frequency, γ is the gyromagnetic ratio, μ_0 the vacuum permeability, and $\alpha_\mathrm{eff} = \alpha + \gamma\mu_0\Delta H_0/(2\omega)$ is the effective damping parameter, with Gilbert damping constant α and inhomogeneous broadening ΔH_0. The out-of-plane resonance condition for our films obeys $\omega = \gamma\mu_0(H_\mathrm{res} - M_\mathrm{eff})$.

B. Background Correction

To measure the sample inductance, we acquire the microwave transmission S-parameter $S_{21} \equiv V_{\mathrm{in},2}/V_{\mathrm{out},1}$ where $V_{\mathrm{in(out)},1(2)}$ is the voltage input (output) at port 1 (2) of the VNA. We fit the raw FMR spectra to:

$$S_{21}(\omega, H_0) = Ae^{i\phi}\chi_{yy}(\omega, H_0) + C_0 + C_1 H_0 \tag{M16}$$

where A is the signal amplitude, ϕ is the raw phase (inclusive of signal line delay), and C_0 and C_1 are complex offset and slope corrections to the background. Utilizing the information in this complex background is key to our data processing method. The background-corrected signal is calculated as:

$$\Delta S_{21}(\omega, H_0) = \frac{Ae^{i\phi}}{C_0 + C_1 H_0}\chi_{yy}(\omega, H_0) \tag{M17}$$

The background correction in Eq. M17 corrects the signal phase for the finite length of the signal line between the VNA source and receiver ports and the sample, effectively placing the ports at the sample position. Additionally, it normalizes the signal amplitude by the frequency-dependent losses due to the complete microwave circuit (cables + CPW + sample). In Fig. S4(a) and (b), we plot the raw and de-embedded data, respectively. The inductance amplitude $\tilde{L}(f)$ is then calculated as $\Delta S_{21}/(\chi_{yy}(\omega, H_0))(-iZ_0/(2\pi f))$ (e.g., Fig. 2 in the main text).

When $\tilde{L}$ is plotted vs. frequency, we note that there can be a small anomalous phase that causes $\mathrm{Im}(\tilde{L})(f \to 0) \neq 0$. This anomalous phase and its correction are discussed in SI Sec. V.

IV. INDUCTANCE DERIVATIONS

A. Inductance due to dipole field of dynamic magnetization

The zeroth-order inductance due to inductive coupling of the CPW to the AC dipolar fields produced by the precessing FM magnetization is derived in Ref. M11.

$$L_0 = \frac{\mu_0 \ell}{W_{\rm wg} d_{\rm FM} I^2} \left[\int_{-\infty}^{+\infty} dy \int_{d_{\rm wg}}^{d_{\rm FM}+d_{\rm wg}} dz \left[\mathbf{q}(y,z) \cdot \chi(\omega, H_0) \cdot \mathbf{h}_1(y,z,I) \right] \right] * \left[\int_{-\infty}^{+\infty} dy \int_{d_{\rm wg}}^{d_{\rm FM}+d_{\rm wg}} dz \left[\mathbf{q}(y,z) \cdot \mathbf{h}_1(y,z,I) \right] \right] \tag{M18}$$

$$\cong \frac{\mu_0 \ell}{W_{\rm wg} d_{\rm FM} I^2} \chi_{yy}(\omega, H_0)\, h_y^2(I,z)\, d_{\rm FM}^2 W_{\rm wg}^2$$

$$\cong \frac{\mu_0 \ell}{W_{\rm wg} d_{\rm FM} I^2} \chi_{yy}(\omega, H_0) \left(\frac{I}{2W_{\rm wg}} \eta(z, W_{\rm wg}) \right)^2 d_{\rm FM}^2 W_{\rm wg}^2$$

$$= \frac{\mu_0 \ell d_{\rm FM}}{4 W_{\rm wg}} \chi_{yy}(\omega, H_0)\, \eta^2(z, W_{\rm wg}) \tag{M19}$$

We have assumed the coordinate system described in Fig. S1 ($\hat{x}$ along the CPW signal propagation direction, $\hat{z}$ along the CPW and sample normal). The function $\mathbf{q}(y,z)$ describes the normalized spatial amplitude of the FMR mode. For the uniform mode, $\mathbf{q}(y,z) = 1$ over the entire sample. The first set of integrals in brackets captures the the integrated amplitude of the mode as excited by the driving microwave field $\mathbf{h}_1 = h_y \hat{y}$, while the second describes the inductive pickup sensitivity of the CPW. The first approximation assumes uniform microwave field over the sample dimensions. The second approximation utilizes the Karlqvist equation to approximate the microwave field as $h_y(I,z) \cong I/(2W_{\rm wg})\eta(z, W_{\rm wg})$, where $\eta(z, W_{\rm wg}) \equiv (2/\pi)\arctan(W_{\rm wg}/2z)$ is the spacing loss due to a finite distance z between sample and waveguide.

B. Mutual Inductance of two current-carrying sheets

Following Rosa[M12], we model the sample and CPW as two thin current-carrying sheets of width w, separation z, and length l, so that the mutual inductance is given by

$$L_{12} = \frac{\mu_0}{4\pi} 2l \left[\ln\left(\frac{2l}{R} \right) - 1 \right] \tag{M20}$$

where R is defined as

$$R \equiv \sqrt{w^2 + z^2} \left(\frac{d}{\sqrt{w^2 + z^2}} \right)^{\left(\frac{z}{w}\right)^2} \exp\left(\frac{2z}{w} \arctan\left(\frac{w}{z} \right) - \frac{3}{2} \right) \tag{M21}$$

C. Inductance due to $\tilde{\sigma}_{\rm NM}$

Viewing the sample-CPW system as a voltage transformer (two mutually-coupled inductors), the voltage induced in the CPW due to current $I_{\rm NM}$ in the NM and the mutual inductance L_{12} is given by $V = -L_{12}(\partial I_{\rm NM}/\partial t)$. If instead we consider the system to be a single lumped-element inductor, the voltage due to the self-inductance contributed by the sample $L_{\rm NM}$ and applied current $I_{\rm CPW}$ is $V = L_{\rm NM}(\partial I_{\rm CPW}/\partial t)$. Therefore, we can calculate $L_{\rm NM}$ as:

$$L_{\rm NM} = -L_{12} \frac{I_{\rm NM}}{I_{\rm CPW}} \tag{M22}$$

The charge current we are interested in is that driven by the magnetization dynamics of the FM layer, and given by the off-diagonal term of Eq. M1:

$$I_{\rm NM} = \hat{x} \cdot \left[\int_{-t_{\rm NM}}^{+d_{\rm FM}} \mathbf{J}(z) dz \right] W_{\rm wg} \tag{M23}$$

$$= \hat{x} \cdot \left[\left(\hat{z} \times (-\sigma_{\rm e}^{\rm F} + \sigma_{\rm e}^{\rm SOT} - \sigma_{\rm o}^{\rm SOT}[\hat{m}\times]) \right) \frac{\hbar}{2e} \partial_t \hat{m} \right] W_{\rm wg} \tag{M24}$$

Assuming a linear solution to the Landau-Lifshitz-Gilbert equation of motion for the magnetization, we write a simple relation between the dynamic component of the magnetization $\mathbf{m}$ and microwave field $\mathbf{h}_1$.

$$\partial_t \hat{m} = i\omega \frac{\chi}{M_{\rm s}} \mathbf{h}_1 \tag{M25}$$

To convert the vector cross products in Eq. M24 to the complex plane, we use χ in the frequency domain[M17].

$$\partial_t \hat{m} = i\omega \frac{\gamma\mu_0}{\omega_{\rm res}^2 - \omega^2 + i\omega\Delta\omega} \begin{bmatrix} \left(1+\alpha^2\right)\omega_y - i\alpha\omega & i\omega \\ -i\omega & \left(1+\alpha^2\right)\omega_x - i\alpha\omega \end{bmatrix} \begin{bmatrix} h_x = 0 \\ h_y \end{bmatrix} \tag{M26}$$

$$\approx i\omega \frac{\gamma\mu_0}{\omega_{\rm res}^2 - \omega^2 + i\omega\Delta\omega} \begin{bmatrix} i\omega \\ \omega_x \end{bmatrix} \tag{M27}$$

where $\omega_{x,y} \equiv \gamma\mu_0 H_{x,y}$, $H_{x,y}$ is the stiffness field in the x or y direction (including external, anisotropy, and demagnetizing fields), $\omega_{\rm res} \equiv \sqrt{\omega_x \omega_y}$, and $\Delta\omega \equiv \alpha(\omega_x + \omega_y)$. The approximation in Eq. M27 drops all terms of order α and α^2, and utilizes the fact that we are only applying microwave fields along y.

Eq. M24 has even terms along $\hat{z} \times \partial_t \hat{m}$ and odd terms along $\hat{z} \times (\hat{m} \times \partial_t \hat{m})$. Using the column vector for $\partial_t \hat{m}$ given by Eq. M27, we can work out these cross products assuming $\hat{m} \parallel \hat{z}$ (small-angle FMR excitation), and then evaluate the $\hat{x}$ projection as prescribed by Eq. M24. If we restrict the analysis to frequencies near resonance, then for circular precession $\omega_x = \omega_{\rm res} \approx \omega$.

$$I_{\rm NM} = \frac{\chi_{yy} h_y}{M_{\rm s}} \left[-\sigma_{\rm o}^{\rm SOT} + i(\sigma_{\rm e}^{\rm F} - \sigma_{\rm e}^{\rm SOT}) \right] \frac{\hbar\omega}{2e} W_{\rm wg} \tag{M28}$$

Finally, from the Karlqvist equation[M18], we approximate the field of the CPW as $h_y = I_{\rm CPW}/(2W_{\rm wg})\eta(z, W_{\rm wg})$. With these substitutions into Eq. M22, we recover $\tilde{\sigma}_{\rm NM} = (\sigma_{\rm o}^{\rm SOT} + i(\sigma_{\rm e}^{\rm SOT} - \sigma_{\rm e}^{\rm F}))$ and Eq. M11.

D. Calculation of $\tilde{\sigma}_{\rm NM}$ from measured L

Using the results for $\mathrm{Re}(\tilde{L})$ and $\mathrm{Im}(\tilde{L})$ (Eqs. M12 and M13), we can isolate the $\tilde{\sigma}_{\rm NM}$ contribution as follows:

$$\frac{d\tilde{L}}{df} = \frac{1}{4} \, \mathrm{sgn}(\hat{z} \cdot \hat{n}) \eta(z, W_{\rm wg}) \frac{L_{12}(z, W_{\rm wg}, l)}{M_{\rm s}} \frac{h}{e} \left[\sigma_{\rm o}^{\rm SOT} + i(\sigma_{\rm e}^{\rm SOT} - \sigma_{\rm e}^{\rm F}) \right] \tag{M29}$$

We normalize $d\tilde{L}/df$ by $\tilde{L}_0$ (where $\tilde{L}_0 \equiv L_0/\chi_{yy}$) in order to remove any residual differences in sample-CPW coupling from sample to sample. The variation in L_0 (evident in Fig. 2) is most likely the result of sample-to-sample variations in magnetization, including dead layer effects at the various Py/NM interfaces, as well as measurement-to-measurement variations in the sample-waveguide spacing, which could be affected by dirt in the measurement environment.

$$\frac{\dfrac{d\tilde{L}}{df}}{\tilde{L}_0} = \mathrm{sgn}(\hat{z} \cdot \hat{n}) \frac{L_{12}(z, W_{\rm wg}, l)}{\mu_0 l} \frac{h}{e} \frac{W_{\rm wg}}{M_{\rm s} d_{\rm FM} \eta(z, W_{\rm wg})} \left[\sigma_{\rm o}^{\rm SOT} + i(\sigma_{\rm e}^{\rm SOT} - \sigma_{\rm e}^{\rm F}) \right] \tag{M30}$$

And finally, solve for the effective conductivity.

$$\left[\sigma_{\rm o}^{\rm SOT} + i(\sigma_{\rm e}^{\rm SOT} - \sigma_{\rm e}^{\rm F}) \right] = \mathrm{sgn}(\hat{z} \cdot \hat{n}) \left(\frac{\dfrac{d\tilde{L}}{df}}{\tilde{L}_0} \right) \frac{\mu_0 l}{L_{12}(z, W_{\rm wg}, l)} \frac{M_{\rm s} d_{\rm FM}}{W_{\rm wg}} \eta(z, W_{\rm wg}) \tag{M31}$$

V. ANALYSIS PROTOCOL

Our quantitative VNA-FMR analysis protocol is summarized below.

1. Complex VNA-FMR data is collected and fit with Eq. M16.
2. ΔS_{21} is calculated with Eq. M17 to de-embed the sample contribution to the inductance.
3. The sample inductance L is calculated using Eq. M9.
4. L is normalized by magnetic susceptibility χ_{yy}, yielding the complex inductance amplitude given by Eqs. M12 and M13 ($\mathrm{Re}(\tilde{L})$ and $\mathrm{Im}(\tilde{L})$).
5. The anomalous phase of $\tilde{L}$ is corrected as described in SI Sec. V.
6. Linear fits of $\tilde{L}(\omega)$ (using Eqs. M12 and M13) are used to extract $\tilde{L}_0$ and $\tilde{L}_{\mathrm{NM}}(\omega)$.
7. The effective conductivities $\sigma_{\mathrm{o}}^{\mathrm{SOT}}$ and $(\sigma_{\mathrm{e}}^{\mathrm{SOT}} - \sigma_{\mathrm{e}}^{\mathrm{F}})$ are calculated from $(\partial\tilde{L}/\partial f)/\tilde{L}_0$ according to Eq. M31.

[M1] F. Freimuth, S. Blügel, and Y. Mokrousov, Physical Review B **92**, 064415 (2015).
[M2] S. Ramo, J. R. Whinnery, and T. V. Duzer, *FIELDS AND WAVES IN COMMUNICATION ELECTRONICS, 3RD ED* (Wiley-India, 2008) google-Books-ID: VFFqU7pXl6gC.
[M3] R. M. White, *Introduction to magnetic recording* (IEEE Press, 1985) google-Books-ID: 4ydTAAAAMAAJ.
[M4] M. Weiler, J. M. Shaw, H. T. Nembach, and T. J. Silva, Physical Review Letters **113**, 157204 (2014).
[M5] C. Hahn, G. de Loubens, M. Viret, O. Klein, V. V. Naletov, and J. Ben Youssef, Physical Review Letters **112**, 179901 (2014).
[M6] L. Onsager, Physical Review **37**, 405 (1931).
[M7] E. Saitoh, M. Ueda, H. Miyajima, and G. Tatara, Applied Physics Letters **88**, 182509 (2006).
[M8] J. C. R. Sánchez, L. Vila, G. Desfonds, S. Gambarelli, J. P. Attané, J. M. De Teresa, C. Magén, and A. Fert, Nature Communications **4**, 2944 (2013).
[M9] D. Wei, M. Obstbaum, M. Ribow, C. H. Back, and G. Woltersdorf, Nature Communications **5** (2014), 10.1038/ncomms4768.
[M10] C. Hahn, G. de Loubens, M. Viret, O. Klein, V. V. Naletov, and J. Ben Youssef, Physical Review Letters **111**, 217204 (2013).
[M11] T. J. Silva, H. T. Nembach, J. M. Shaw, B. Doyle, K. Oguz, K. O'Brien, and M. Doczy, in *Metrology and Diagnostic Techniques for Nanoelectronics*, edited by Z. Ma and D. G. Seiler (Pan Stanford Publishing Pte. Ltd, 2016).
[M12] E. B. Rosa, *The self and mutual inductances of linear conductors* (US Department of Commerce and Labor, Bureau of Standards, 1908).
[M13] M.-H. Nguyen, D. C. Ralph, and R. A. Buhrman, Physical Review Letters **116**, 126601 (2016).
[M14] Y. Niimi, M. Morota, D. H. Wei, C. Deranlot, M. Basletic, A. Hamzic, A. Fert, and Y. Otani, Physical Review Letters **106**, 126601 (2011).
[M15] J. Sinova, S. O. Valenzuela, J. Wunderlich, C. H. Back, and T. Jungwirth, Reviews of Modern Physics **87**, 1213 (2015).
[M16] M. Bailleul, Applied Physics Letters **103**, 192405 (2013).
[M17] M. L. Schneider, J. M. Shaw, A. B. Kos, T. Gerrits, T. J. Silva, and R. D. McMichael, Journal of Applied Physics **102**, 103909 (2007).
[M18] J. C. Mallinson, *The Foundations of Magnetic Recording* (Academic Press, 2012) google-Books-ID: wIXIy0hIAHoC.

Supplementary Information for "Evidence for a common origin of spin-orbit torque and the Dzyaloshinskii-Moriya interaction at a $Ni_{80}Fe_{20}$/Pt interface"

I. EXPERIMENTAL SETUP

The FM/NM sample is inductively coupled to a microwave coplanar waveguide (CPW). The flux generated by the bilayer sample arises from four distinct sources: (1) the magnetization dynamics in the FM, which produce an oscillating dipolar field $H_{\rm dipole}$ at the CPW, (2) the AC current induced in the NM by the Faraday effect from the FM, which in turn produces an oscillating (and time-reversal even) Oersted field $H_{\rm e}^{\rm F}$ at the CPW, (3) the AC current produced in the NM from odd (damping-like) SOT effects (e.g., spin pumping + spin Hall), which produces an Oersted field $H_{\rm o}^{\rm SOT}$, and (3) the AC current produced at the NM/FM interface from even (field-like) SOT effects (e.g., Rashba-Edelstein), which produces an Oersted field $H_{\rm e}^{\rm SOT}$.

Figure S1(b) and (c) show schematics of these four signal sources at two instants in time: when the dipolar and odd SOT effects are maximal (Fig. S1(b)) and when the Faraday and even SOT effects are maximal (Fig. S1(c)). Fig. S1(d) shows the time dependence of the signal-generating component of each source and its time derivative, the latter being proportional to induced voltage in the CPW. These plots show each SOT source has a distinct phase relationships to the driving field $h_{\rm y}$, which we exploit below to determine their contributions separately.

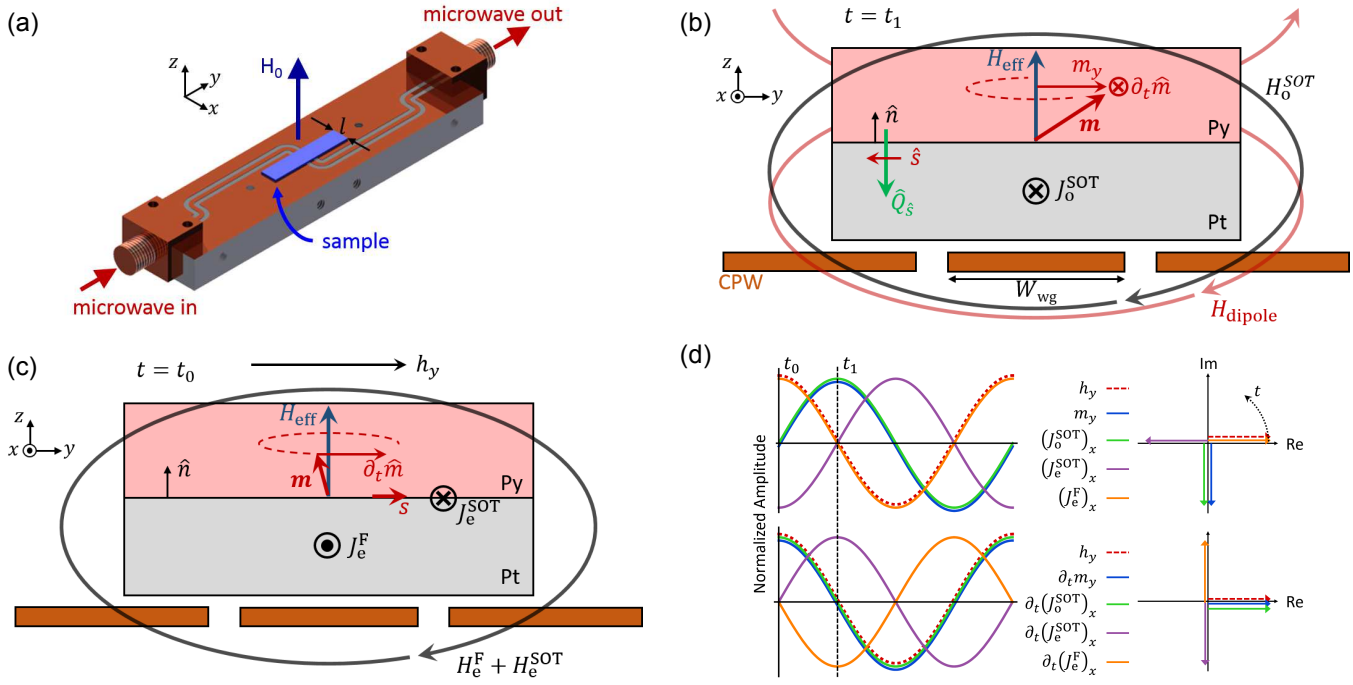

Figure S1. (a) Flip-chip sample on CPW, showing out-of-plane field H_0 and sample length l. Microwave driving field points primarily along $\hat{y}$ at the sample. (b) Schematic of the bilayer, with coordinate system, precessing magnetization $\mathbf{m}(t)$, odd-symmetry SOT current $J_{\rm o}^{\rm SOT}$ (e.g., due to spin Hall effect), and the dynamic fields produced by each ($H_{\rm dipole}$ and $H_{\rm o}^{\rm SOT}$) at time t_1 when $\mathbf{m} = \langle 0, m_y, m_z \rangle$. Interface normal $\hat{n}$, spin orientation $\hat{s}$, and spin flow direction $\hat{Q}_{\hat{s}}$ due to spin pumping into the Pt are also shown. Bilayer is insulated from CPW using photoresist spacer layer (not shown). (c) Same as (b), except at time t_0 when $\mathbf{m} = \langle m_x, 0, m_z \rangle$. In this case, there is no spin Hall contribution to J_x, $J_{\rm e}^{\rm F}$ and $J_{\rm e}^{\rm SOT}$ (e.g., due to Rashba-Edelstein effect) are maximal along $\pm\hat{x}$, and the spin accumulation (with orientation $\hat{s}$) and $J_{\rm e}^{\rm SOT}$ are produced at the Py/Pt interface. (d) Amplitude of driving field h_y and different signal sources as a function of time (left), and viewed in the complex plane at time t_0 (right). Relative amplitudes not indicated. Note that currents and Py magnetization (top panel) are 90° shifted from the voltages they produce in the CPW ($\propto d\Phi/dt$, bottom panel).

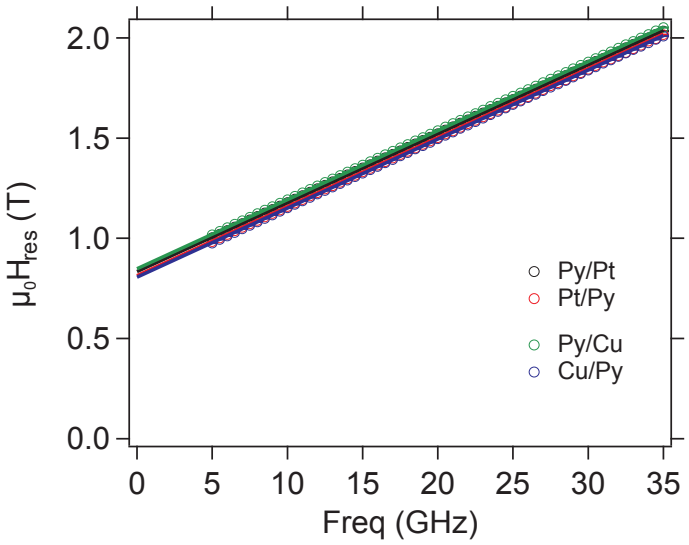

Figure S2. Resonance field vs. frequency dispersion, to extract spectroscopic g-factor, and M_{eff}.

II. MAGNETIC CHARACTERIZATION

The frequency dependence of the resonant field H_{res} and linewidth ΔH allow extraction of the effective magnetization $M_{\text{eff}} = M_{\text{s}} - H_{\text{k}}^{\perp}$ (where $H_{\text{k}}^{\perp}$ is the perpendicular anisotropy), spectroscopic g-factor g, inhomogeneous broadening ΔH_0, and Gilbert damping parameter α. We used SQUID magnetometry to measure the magnetization per unit area for all samples. Magnetization, g-factor, and damping values are summarized in Table I.

A. Resonance Field Dispersion

From the susceptibility fits to the S_{21} spectra, we extract the resonance field as a function of microwave frequency. This is expected to follow the Kittel dispersion for out-of-plane field H_0.

$$\omega = \mu_0 \gamma (H_{\text{res}} + M_{\text{eff}}) \tag{S1}$$

A plot of $\mu_0 H_{\text{res}}$ vs. $f = \omega/2\pi$ is shown in Fig. S2, with slope set by the gyromagnetic ratio $\gamma = g\mu_{\text{B}}/\hbar$, and y-intercept set by $\mu_0 M_{\text{eff}}$.

B. Linewidth and Damping

The resonance linewidth is determined by the Gilbert damping constant α and inhomogeneous broadening ΔH_0 according to

$$\mu_0 \Delta H = \mu_0 \Delta H_0 + \frac{2\omega\alpha}{\gamma} \tag{S2}$$

Data and fits of Eq. S2 for the 6 mm long samples for each deposition order are shown in Fig. S3. The signal-to-noise ratio for the Pt/Py sample degrades since the contributions from magnetization dynamics (L_0) and odd inverse spin orbit torque ($\sigma_{\text{o}}^{\text{SOT}}$) add destructively and the signal amplitude trends towards zero as $f \to 35\,\text{GHz}$.

C. Background Correction

An example of the fit described by Eq. M16 is shown in Fig. S4(a). Note the large complex offset on top of which the resonance signal is superimposed. De-embedded data following background correction are plotted in panel (b).

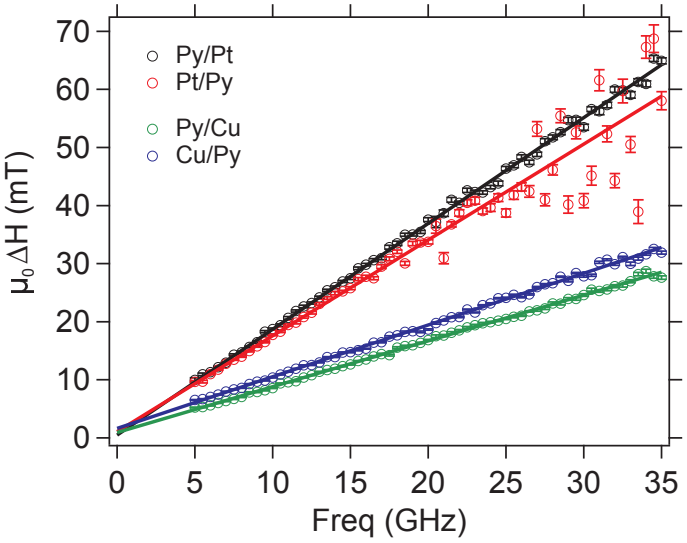

Figure S3. Resonance linewidth vs. frequency, to extract Gilbert damping constant α and inhomogeneous broadening.

Sample	M_{eff} (kA/m)	g	$\mu_0 \Delta H_0$(mT)	α	$M_s d_{\text{FM}}$ (μA)
Py/Pt	663.5 ± 0.7	2.079 ± 0.001	1.2 ± 0.8	0.0261 ± 0.0003	2069 ± 1
Pt/Py	647 ± 1	2.079 ± 0.003	2 ± 2	0.0241 ± 0.0008	2121 ± 1
Py/Cu	674 ± 1	2.075 ± 0.001	1.1 ± 0.5	0.0115 ± 0.0001	2341 ± 2
Cu/Py	642 ± 1	2.077 ± 0.001	1.7 ± 0.9	0.0129 ± 0.0002	2077.0 ± 0.4

Table I. FMR and SQUID parameters for Py/Pt and Py/Cu bilayers.

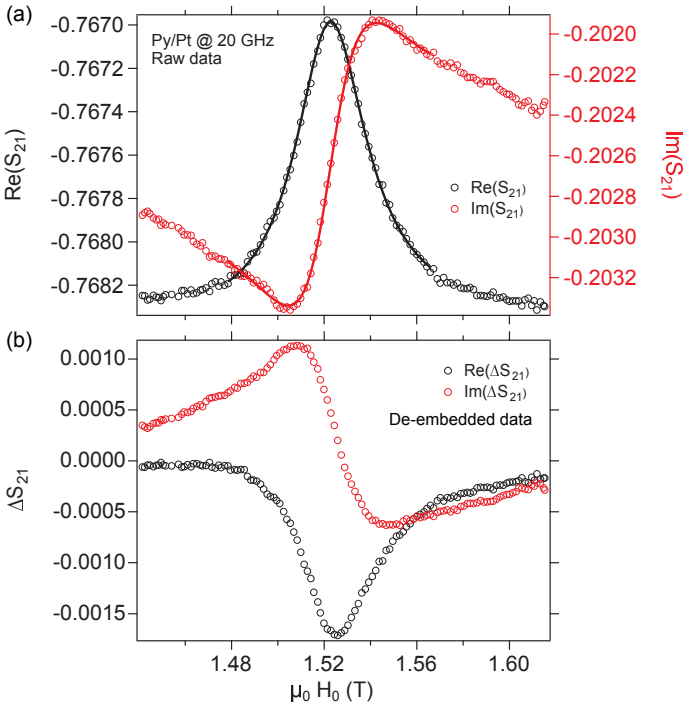

Figure S4. Example S_{21} spectrum, acquired at f = 20.0 GHz. (a) Raw data, with fits. Note the different background offsets of the Re and Im data (left and right axes). (b) De-embedded ΔS_{21} signal.

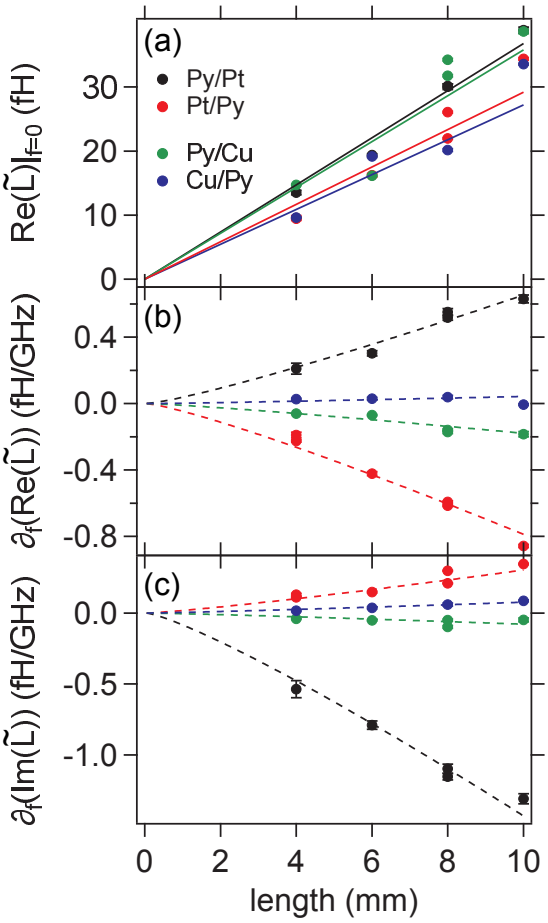

Figure S5. $\tilde{L}(f=0)$ and $\partial\tilde{L}/\partial f$ extracted from data as in Fig. 2 vs. sample length for all samples. (a) Dipolar inductive coupling $\tilde{L}_0$. (b) From $\partial[\mathrm{Re}(\tilde{L})]/\partial f$, we extract $\sigma_\mathrm{o}^\mathrm{SOT}$ and SHE. (c) From $\partial[\mathrm{Im}(\tilde{L})]/\partial f$, we extract $(\sigma_\mathrm{e}^\mathrm{SOT}-\sigma_\mathrm{e}^\mathrm{F})$ and REE. Dashed lines are guides based on Eqs. M8 and M9 with values of $\sigma_\mathrm{o}^\mathrm{SOT}$ and $(\sigma_\mathrm{e}^\mathrm{SOT}-\sigma_\mathrm{e}^\mathrm{F})$ calculated as described in the Methods. Several measurements were repeated to demonstrate reproducibility.

D. SQUID Measurement

We measured in-plane hysteresis curves at room temperature to determine the saturation moment of our samples. This total moment was normalized by the sample area to obtain $M_\mathrm{s}d_\mathrm{FM}$.

III. SAMPLE INDUCTANCE VS. LENGTH

Each of the inductance terms has some dependence on sample length: linear for the dipolar contribution, and slightly non-linear for the inductances due to charge flow in the NM (see Eqs. M19 and M20). We therefore repeated the measurements shown in Fig. 2 for a variety of sample lengths from 4 to 10 mm. Fig. S5 shows the measured inductance terms L_0, $\partial\mathrm{Re}(L)/\partial f$ (intercept and slope of curves in Fig. 2(a)), and $\partial\mathrm{Im}(L)/\partial f$ (slope of curves in Fig. 2(b)) as a function of sample length. Following normalization by its corresonding $\tilde{L}_0$, each data point in Fig. S5(b) provides a value of $\sigma_\mathrm{o}^\mathrm{SOT}$ (see Eq. M31). Similarly, data points in panel (c) provide values of $(\sigma_\mathrm{e}^\mathrm{SOT}-\sigma_\mathrm{e}^\mathrm{F})$. These values are averaged to provide a single $\sigma_\mathrm{o}^\mathrm{SOT}$ and $(\sigma_\mathrm{e}^\mathrm{SOT}-\sigma_\mathrm{e}^\mathrm{F})$ for each sample type. Results are summarized in Table 1. The dashed lines in Fig. S5(b) and (c) are calculated curves based on these average values.

IV. RELATIONSHIP OF SPIN-ORBIT TORQUES AND MICROSCOPIC SPIN-CHARGE CONVERSION PARAMETERS

For the following calculations of the microscopic parameters associated with the measured SOT conductivities, we make use of the fact that the transduction between the sample and CPW allows for direct measurement of the AC charge currents generated in the samples, not steady-state voltages, as were measured in previous studies[S1,S2]. As such, it is not necessary for us to compensate for current shunting between the FM and NM layers in the sample that attenuates the measured signal in a manner that can be empirically difficult to accurately characterize; e.g., see Eq. 15 in Ref. S3.

A. Spin Hall angle and $\sigma_{\rm o}^{\rm SOT}$

We assume series resistors $1/G_{\uparrow\downarrow} + 1/G_{\rm ext}$ (interfacial spin-mixing conductance + spin conductance of the NM) in a voltage divider model for the spin accumulation at the FM/NM interface due to spin pumping

$$\frac{\mu_{\rm s}(z=0^+)}{e}\hat{s} = \frac{\hbar}{2e}\left(\hat{m}\times\frac{\partial\hat{m}}{\partial t}\right)\left(\frac{G_{\uparrow\downarrow}}{G_{\uparrow\downarrow}+G_{\rm ext}}\right) \tag{S3}$$

where $\mu_{\rm s}(z=0^+)$ is the spin accumulation at the FM/NM interface. Using the result of Eq. 6 from Ref. S4 for the effective one-dimensional spin conductance of a NM (where we have set $G_2^{\rm NM}=0$ because we are interested in only a FM/NM bilayer, not a FM/NM1/NM2 multilayer):

$$G_{\rm ext} = \frac{G_{\rm Pt}}{2}\tanh\left(\frac{d_{\rm Pt}}{\lambda_{\rm s}}\right) \tag{S4}$$

where $G_{\rm Pt}\equiv\sigma_{\rm Pt}/\lambda_{\rm s}$ and $\lambda_{\rm s}$ is the spin diffusion length in the Pt. The integrated charge current in the Pt layer driven by the resulting spin chemical potential gradient $\partial\mu_{\rm s}/\partial z$ and the inverse spin Hall effect is given by

$$\int_0^{d_{\rm Pt}} J_{\rm c}(z)dz = \int_0^{d_{\rm Pt}}\left[\sigma_{\rm SH}\frac{\partial\mu_{\rm s}(z)/e}{\partial z}\right]dz \tag{S5}$$

$$= \sigma_{\rm SH}\frac{\mu_{\rm s}(z=0^+)}{e} \tag{S6}$$

assuming $d_{\rm Pt} >> \lambda_{\rm s}$. The spin Hall conductivity is related to the spin Hall angle via the Pt charge conductivity: $\sigma_{\rm SH} = \theta_{\rm SH}\sigma_{\rm Pt}$. If we combine Eqs. S3, S4, and S6 and equate the integrated charge current to that from $\sigma_{\rm o}^{\rm SOT}$ in Eq. M8 we arrive at the final result:

$$\sigma_{\rm o}^{\rm SOT} = \theta_{\rm SH}\sigma_{\rm Pt}{\rm Re}\left[\frac{G_{\uparrow\downarrow}}{\frac{\sigma_{\rm Pt}}{2\lambda_{\rm s}}\tanh\left(\frac{d_{\rm Pt}}{\lambda_{\rm s}}\right)+G_{\uparrow\downarrow}}\right](1-\delta) \tag{S7}$$

where $G_{\uparrow\downarrow}$ is the spin mixing conductance, $\sigma_{\rm Pt}$, $\lambda_{\rm s}$, and $d_{\rm Pt}$ are the conductivity, spin diffusion length, and thickness of the Pt layer, respectively. We used the spin transport parameters obtained via spin pumping measurements with Py/Pt bilayers in Ref. S5, wherein the data were fit with a model that assumed a constant spin diffusion length with varying NM film thickness, as originally suggested by Jiao and Bauer[S3]. The fitting model also accounted for spin memory loss at the Py/Pt interface (δ is the interfacial spin loss fraction). Therefore, we use: $\sigma_{\rm Pt}$ =$4.4\times10^6\,\Omega^{-1}{\rm m}^{-1}$, $\lambda_{\rm sf}$ =0.37 nm, $G_{\uparrow\downarrow}$ =$2.65\times10^{15}\,\Omega^{-1}{\rm m}^{-2}$, and $\delta = 0.3$. Addtionally, we replace the left-hand side of Eq. S7 with $(\sigma_{\rm o}^{\rm SOT})_{\rm Py/Pt} - (\sigma_{\rm o}^{\rm SOT})_{\rm Py/Cu}$ in order to remove any residual effects from the Ta interfaces.

Sample	$\phi_{\rm corr}$ (deg)
Py/Pt	12 ± 1
Pt/Py	11.6 ± 0.4
Py/Cu	1.8 ± 0.8
Cu/Py	7.2 ± 0.3

Table II.

B. Rashba parameter and $\sigma_{\rm e}^{\rm SOT}$

To relate the even spin-orbit torque conductivity $\sigma_{\rm e}^{\rm SOT}$ to the Rashba parameter, we start from the field-like interfacial spin torque per spin introduced by Kim, et al. (Eq. 12 in Ref. S6):

$$\mathbf{t}_{\rm fl} = {\rm sgn}(\hat{z}\cdot\hat{n}) k_{\rm R} v_{\rm s} \left[\hat{m}\times(\hat{j}\times\hat{z})\right]\left(\frac{\hbar}{2}\right) \tag{S8}$$

where $k_{\rm R} = 2\alpha_{\rm R} m_{\rm e}/\hbar^2$ is a wavevector corresponding to the Rashba energy parameter $\alpha_{\rm R}$, and $v_{\rm s} = PJg\mu_{\rm B}/(2eM_{\rm s})$ is the spin velocity, with charge current density J, and spin polarization of the charge current P. Note that $\mathbf{t}_{\rm fl}/(\hbar/2)$ has units of Hz; that is, the same units as $\partial_t\hat{m}$. We can therefore relate Eq. S8 to the volume-averaged magnetic torque density $\mathbf{T}$ from Eq. M7 through the time rate of change of the magnetization: $\mathbf{t}_{\rm fl} d_{\rm int}\delta(z)/(\hbar/2) = \partial_t\hat{m}$, where we have added $d_{\rm int}\delta(z)$ to account for the interfacial nature of this torque (where $d_{\rm int}$ is an effective thickness of the interface).

$$\frac{2}{\hbar}\int_0^{d_{\rm FM}} \mathbf{t}_{\rm fl} d_{\rm int}\delta(z)dz = -\frac{\gamma}{M_{\rm s}}\int_0^{d_{\rm FM}} \mathbf{T}(z)dz \tag{S9}$$

$$k_{\rm R} v_{\rm s}\hat{m}\times(\hat{j}\times\hat{z}) d_{\rm int} = -\frac{\gamma}{M_{\rm s}}\frac{\hbar}{2e}\sigma_{\rm e}^{\rm SOT}\hat{m}\times(\hat{z}\times\mathbf{E}) \tag{S10}$$

where the final line results from subsituting Eq. S8 and the even SOT term from Eq. M7 into Eq. S9. Making the substitutions for $k_{\rm R}$ and $v_{\rm s}$, and using $\mathbf{E} = (J\rho_{\rm int}/d_{\rm int})\hat{j}$ (where $\rho_{\rm int}/d_{\rm int} = 1/\sigma_{\rm int}$ and $\rho_{\rm int}$ has units of $\Omega{\rm m}^2$) yields Eq. 4 in the main text. We can also express the magnitude of the interfacial field-like torque per spin $t_{\rm fl} = |\mathbf{t}_{\rm fl}|$ as:

$$t_{\rm fl} = -\frac{\gamma}{M_{\rm s}}\frac{\hbar^2}{4e}\sigma_{\rm e}^{\rm SOT}\frac{J\rho_{\rm int}}{d_{\rm int}^2} \tag{S11}$$

V. ANOMALOUS PHASE OF ΔS_{21}

The background correction procedure of Methods Sec. II E requires one further phase correction in order to enforce that ${\rm Im}(\tilde{L})(f=0) = 0$, as any finite ${\rm Im}(\tilde{L})$ at zero frequency would be unphysical. However, as can be seen in the raw data of Fig. S6, the intercept of ${\rm Im}(\tilde{L})$ at $f = 0$ is indeed a small, finite number (left panels). In addition to the background phase correction described in Eq. M17, we therefore force an additional phase correction $\phi_{\rm corr} = \arctan[{\rm Im}(\tilde{L})(f=0)/{\rm Re}(\tilde{L})(f=0)]$. The $\phi_{\rm corr}$ necessary for each sample is shown in Table II. We suspect that this additional phase factor is caused by some capacitive coupling between the sample and CPW, which would violate the simple model we have assumed in which the sample makes a purely inductive contribution to ΔS_{21}. Variation from sample to sample could be caused by wafer-to-wafer variation in the doping of the Si substrate, or small changes in z, the sample-CPW spacing.

VI. FINITE SIZE EFFECTS

We also measured samples with $l = 2\,{\rm mm}$, but found the results to be less reliable than longer samples. We suspect that, because the charge currents flowing in the sample require a return path, the current flow direction will deviate from $\hat{x}$ near the sample edges. These finite size effects will affect the mutual inductance terms, but not the zero-th order inductance (which is not caused by current flows in the sample). As such, the expected inductance behavior described by the $\tilde{\sigma}_{\rm NM}$ terms in Eqs. M12 and M13 breaks down for small samples.

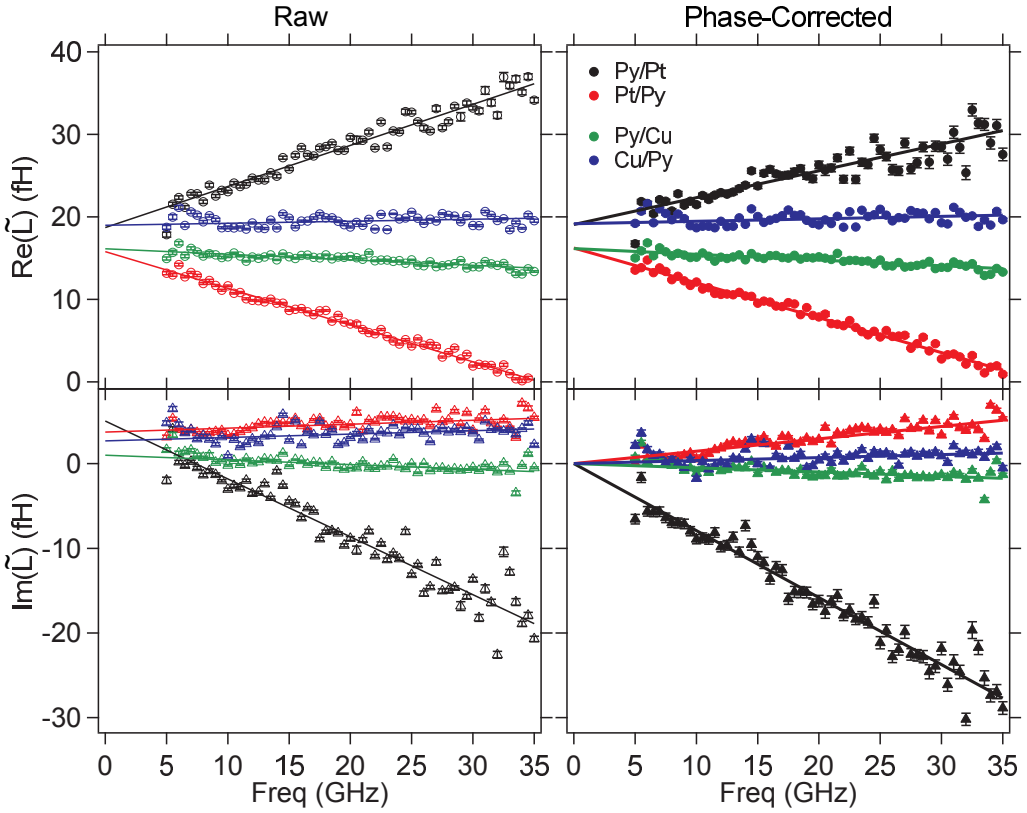

Figure S6. Correction of phase to enforce $\mathrm{Im}(\tilde{L})(f=0)=0$ for $l=6\,\mathrm{mm}$ sample. Raw data (left panels) show a small, non-zero component of $\mathrm{Im}(\tilde{L})$ at $f=0$, which is unphysical. We therefore apply a small correction to eliminate this non-zero y-intercept, resulting in the phase-corrected data (right panels).

VII. MEASUREMENT OF PERMALLOY INTERFACIAL RESISTIVITY

In order to determine the interface resistivity ρ_{int} used for determination of α_{R} in main text Eq. 4, we measured the resistivity of Py films as a function of film thickness. We use Matthiessen's rule to describe the electron scattering rate responsible for the film resistivity as the sum of a bulk scattering rate and interfacial scattering rate. Within a mean free path λ of the Py interfaces (top and bottom):

$$\frac{1}{\tau}=\frac{1}{\tau_{\mathrm{bulk}}}+\frac{1}{\tau_{\mathrm{int}}} \tag{S12}$$

Far from the interface $1/\tau=1/\tau_{\mathrm{bulk}}$. We take a volume average over the film thickness.

$$\left\langle\frac{1}{\tau}\right\rangle\approx\frac{1}{d_{\mathrm{Py}}}\int_0^{d_{\mathrm{Py}}}\left[\frac{1}{\tau_{\mathrm{bulk}}}+\frac{1}{\tau_{\mathrm{int}}}\lambda\left(\delta(z)+\delta(z-d_{\mathrm{Py}})\right)\right]dz \tag{S13}$$

$$=\frac{1}{\tau_{\mathrm{bulk}}}+\frac{2}{\tau_{\mathrm{int}}}\frac{\lambda}{d_{\mathrm{Py}}} \tag{S14}$$

where the δ functions in Eq. S13 account for presence of of interfacial scattering at the top and bottom of the Py film. The film resistivity is given by the usual $\rho=m_{\mathrm{e}}/(ne^2\tau)$. Using the volume-averaged result for $\langle 1/\tau\rangle$, we derive the expected thickness dependence of the film resistivity.

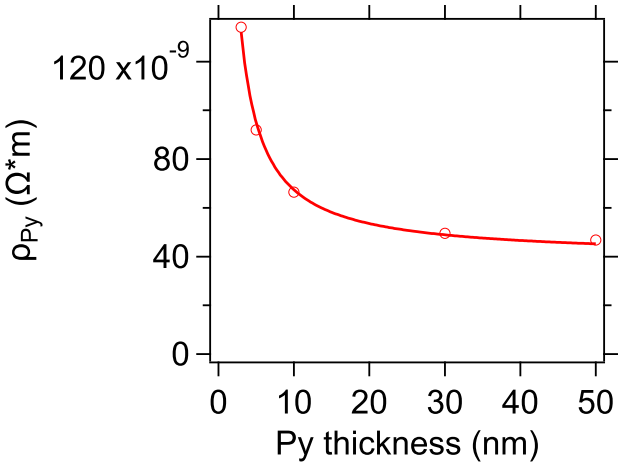

Figure S7. Resistivity vs. thickness for sputtered Py on Ta(1.5 nm) with Ta(1.5 nm) capping layer. Eq. S17 is used as the fit function.

$$\rho = \frac{m_e}{ne^2}\left\langle\frac{1}{\tau}\right\rangle \tag{S15}$$

$$= \frac{m_e}{ne^2}\left(\frac{1}{\tau_{\rm bulk}} + \frac{2}{\tau_{\rm int}}\frac{\lambda}{d_{\rm Py}}\right) \tag{S16}$$

$$= \rho_0 + \frac{2\rho_{\rm int}}{d_{\rm Py}} \tag{S17}$$

where $\rho_{\rm int} \equiv m_e\lambda/(ne^2\tau_{\rm int})$. Using Eq. S17 to fit the data in Fig. S7, we find $\rho_0 = 4.0 \pm 0.2 \times 10^{-8}\,\Omega\,\mathrm{m}$ and $\rho_{\rm int} = 1.39 \pm 0.05 \times 10^{-16}\,\Omega\mathrm{m}^2$.

[S1] M. Weiler, J. M. Shaw, H. T. Nembach, and T. J. Silva, Physical Review Letters **113**, 157204 (2014).
[S2] D. Wei, M. Obstbaum, M. Ribow, C. H. Back, and G. Woltersdorf, Nature Communications **5** (2014), 10.1038/ncomms4768.
[S3] H. Jiao and G. E. W. Bauer, Physical Review Letters **110**, 217602 (2013).
[S4] C. T. Boone, H. T. Nembach, J. M. Shaw, and T. J. Silva, Journal of Applied Physics **113**, 153906 (2013).
[S5] C. T. Boone, J. M. Shaw, H. T. Nembach, and T. J. Silva, Journal of Applied Physics **117**, 223910 (2015).
[S6] K.-W. Kim, H.-W. Lee, K.-J. Lee, and M. D. Stiles, Physical Review Letters **111**, 216601 (2013).

This figure "ExptSchematic_even.png" is available in "png" format from:

http://arxiv.org/ps/1611.05798v1

This figure "ExptSchematic_odd.png" is available in "png" format from:

http://arxiv.org/ps/1611.05798v1

This figure "RenderedCPW_v3.png" is available in "png" format from:

http://arxiv.org/ps/1611.05798v1

This figure "SignalPhases_v3.png" is available in "png" format from:

http://arxiv.org/ps/1611.05798v1